Can Weathering of Banded Iron Formations Generate Natural Hydrogen? Evidence from Australia, Brazil and South Africa

Ugo Geymond, Erick Ramanaidou, Dan Lévy, Abderrahim Ouaya, Isabelle Moretti

Can Weathering of Banded Iron Formations Generate Natural Hydrogen? Evidence from Australia, Brazil and South Africa

Ugo Geymond [1], Erick Ramanaidou [2], Dan Lévy [1], Abderrahim Ouaya [3] and Isabelle Moretti [1,*]

1. Laboratoire des Fluides Complexes et leurs Réservoirs (LFCR)—E2S UPPA, Université de Pau et des Pays de l'Adour, 64012 Pau, France; geymond@ipgp.fr (U.G.); dan.levy@univ-pau.fr (D.L.)
2. Commonwealth Scientific and Industrial Research Organisation (CSIRO), Kensington, WA 6151, Australia; erick.ramanaidou@csiro.au
3. Laboratoire des Sciences du Climat et de l'Environnement (LSCE), IPSL, CEA-CNRS-UVSQ, Université Paris-Saclay, 91190 Gif-sur-Yvette, France; abderrahim.ouaya@universite-paris-saclay.fr
* Correspondence: isabelle.moretti@univ-pau.fr

Abstract: Oxidation of iron-rich rock is known to generate H_2 in oceanic as well as in continental domains. Here we tested the possibility of H_2 generation as the result of weathering of banded iron formations (BIF). The BIF constitute more than 60% of global iron ore reserves with low Fe^{3+}/Fe_{tot} and total Fe ranging from 20 to 40 wt% and are therefore good candidates for H_2 production potential. In the vicinity of BIF-hosted iron mines in Australia, Brazil and South Africa, satellite imaging has revealed the presence of sub-circular depressions that usually are the proxy of H_2-emitting features. A morphological comparison of the sub-circular depressions with the ones observed in previous studies point to probable H_2 seeping in these areas. In parallel, a petrological study conducted on altered and fresh BIF samples from the Hamersley Province in Western Australia also suggests H_2 generation during BIF weathering. Indeed, mineral transitions from ferrous silicate (riebeckite and/or minnesotaite) to ferric iron oxi-hydroxides (goethite) or from ferrous and ferric oxides (magnetite) to exclusively ferric oxides (maghemite, hematite, goethite) were observed on the samples. The oxidation of ferrous iron by aqueous fluids circulating through and leaching the BIF is promising for H_2 generation. The BIF weathering profile suggests that the limiting factor is the presence of water, and that this reaction is happening at, or near, surface temperature. This challenges the idea that high temperatures are required to generate H_2 as it is the case during the serpentinization. The link between BIF and H_2 will have however to be further investigated to better constrain the reactions and their kinetics.

Keywords: natural hydrogen; banded iron formation; iron mine; Australia; South-Africa

1. Introduction

1.1. Global Context

Ongoing ecological transition and society's decarbonization have pushed dihydrogen (H_2) under the spotlight, as it has the desired qualities to be a clean energy source, and especially a clean fuel, as it emits no CO_2 during combustion and it has a high calorific power [1,2]. The demand for H_2 to play a role in the energy mix of tomorrow is high, and almost all countries have now a hydrogen road map. However, H_2 is currently mainly produced by polluting processes and used as raw material. Its green mobility is only starting and, as such, natural H_2 as an energy source or vector is becoming more investigated.

First described at the end of the 1970's offshore along the mid-oceanic ridges, H_2 emissions in an oceanic context have been abundantly studied for 40 years [3–5]. The serpentinization process is consequently well known, leading to the oxidation of Fe^{2+} contained in ferromagnesian minerals found in oceanic lithosphere associated with the reduction of water leading to H_2 generation.

In the past decade, studies revealed that H_2 emissions also occur in a continental context and have been described on wells [6,7] or seeps at the ground level [8–10], especially in intracratonic areas [11–14]. There are numerous proposed sources of H_2, and the more studied ones are (1) iron oxidation and water reduction, (2) radiolysis, (3) radio-mechanical and (4) primordial H_2. Because (1) is the more accepted mechanism leading to H_2 generation, targeting Fe-rich lithologies that could be oxidized can be a good proxy to look for H_2-releasing zones in continental domains.

1.2. An Iron Rich Facies: The Banded Iron Formations

Banded Iron Formations (BIF) are Precambrian sedimentary rocks of marine origin, present in cratonic areas found in all continents [15,16]. Radiochronologic dating showed that they formed during two periods in Earth's history: 3500–1800 My (Archean and mainly Proterozoic) and 900–500 My (Neoproterozoic) [17]. It is generally accepted that they precipitated from ferrous iron previously dissolved in oceanic waters as Fe^{2+}(aq) and transformed in Fe^{3+} by cyanobacteria producing oxygen or via photoferritroph organisms [18]. For the Neoproterozoic BIF, the precipitation might be related to the oxygenation of oceans during interglacier cycles of the Snowball Earth, after long times of anoxia created by the covering of oceans by ice [19].

Today, BIF constitute the biggest iron ore reserves, with the presence of both ferric and ferrous iron, reaching more than 60% of global iron reserves on Earth [20]. Currently, metallurgy compagnies mostly extract iron from BIF (about 90% of total iron production) as in Australia, Brazil, China or India among others. They focus on BIF-hosted ores, where iron content is higher (up to 68 wt%; [21]) and exclusively ferric. In parallel, the iron content in non-weathered BIF is lower (from 20 to 40 wt%; [22]) but highly ferrous and thus appears very promising for H_2 generation by redox reaction.

1.3. Proxy of H_2 Emanations: Sub-Circular Depressions

Sub-circular depressions (SCD), also called "fairy circles" [12], have been described on the surface of unconsolidated sedimentary layer, covering a much older basement of Precambrian origin. In some cases, the presence of H_2 in these SCD have been proven and we will hence call them P_H_2_SCD. In other cases, the presence of H_2 has not been proven yet and we will hence just call them SCD. So far, assumptions have been made that these features represent the morphological expression in the landscape of a deeper on-going H_2 generation or leakage, even if these features and the related H_2 emissions can vary in space and time [23,24].

Over the past 10 years, works in continental domain have focused on these SCD-emitting H_2, which are now observed worldwide, and P_H_2_SCD has been described in the North American [10], Russian [25], Brazilian [9,13] and Western Australian cratons [12,26,27]. A statistical work based on SCD in Russia, Australia and Brazil showed that they can be discriminated from other circular depressions such as karstic features by studying their morphology [12]. Other features, characterized by a rather circular gap of vegetation and also called fairy circles, have been described in Namibia [28], but they are flat and often smaller and so can be differentiated from the gas emitting structures.

Thus, the mapping of the SCD is valuable to track the emissions of H_2 and start an exploration process through a remote sensing survey of the basins. The spatial correlation between the high density of the SCD and Archean or Neoproterozoic cratons has also been noticed by previous authors [12] (Figure 1) and raises the question of the origins of H_2 emissions in intracratonic areas.
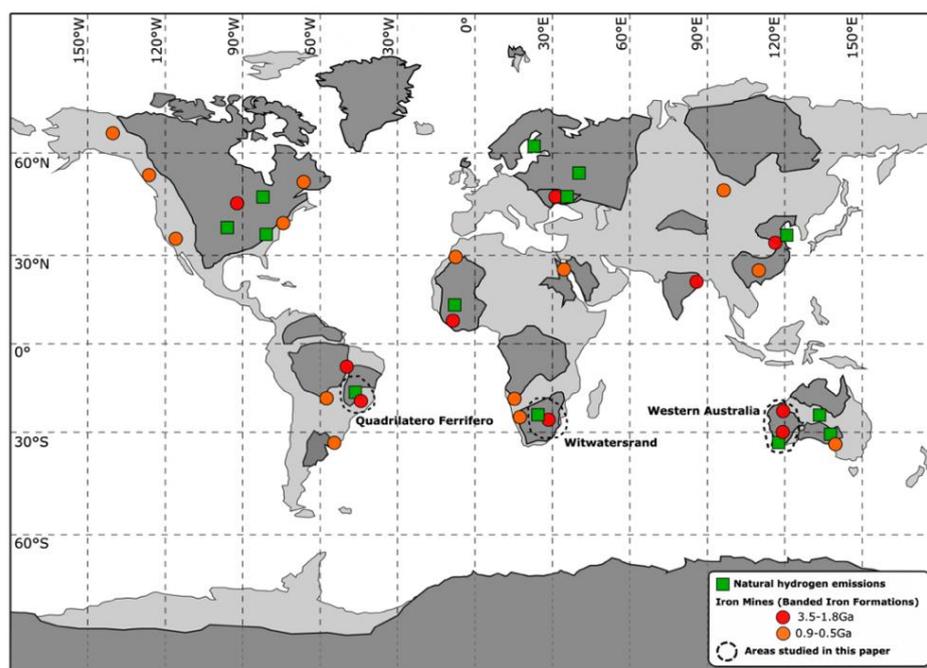
Figure 1. World map of the Precambrian cratons and locations of the study areas. Dark grey corresponds to Precambrian cratons.

1.4. Aim of the Study

In this paper, we explore a possible source rock type for H_2 generation in cratonic areas: reduction of water during oxidation of ferrous minerals in BIF. We focus here on three areas located in Australia, Brazil and South Africa, and two complementary approaches are used to characterize the link between H_2 releases and BIF.

At a large scale, a spatial correlation study is conducted on the presence of sub-circular depressions mapped in the vicinity of iron mines or outcropping BIF in the areas of interest (Figure 1), based on satellite imaging. Their characteristics in terms of size and footprint are compared with those of the P_H_2_SCD with measured H_2 emanations published previously in Australia, Brazil and Russia [12].

Secondly, the potential for H_2 production through BIF oxidation is evaluated. To do so, available data in literature are discussed, and results of our petrological study conducted on BIF samples from Australia are presented. The possibility to have an oxidation and therefore H_2 production near the surface, involving very low temperature of generation, will be discussed.

2. Study Locations and Geological Settings

2.1. Australia

Australia is subdivided into three major Precambrian cratonic units, respectively: the North Australian Craton, West Australian Craton and South Australian Craton (Figure 2). Older terranes such as Yilgarn, Pilbara or Gawler are assumed to have collided from 1800 to 1100 Ma during the make-up of Rodinia and resulted in the formation of Proterozoic orogenesis terranes. During the late Proterozoic, several rifting cycles associated with the break-up of the supercontinent resulted in the formation of Proterozoic basins such as Adelaide [29,30]. Nowadays, these cratons constitute the basement, outcropping or covered by younger layers of Phanerozoic ages. They contain a diversity of rocks, from sedimentary to igneous intrusive and extrusive. These rocks constitute a vast reservoir of raw material, including rare earth elements, gold or iron ore. The latter is mined in BIF-hosted iron ores, mainly in Western Australia, making Australia the first iron ore producer worldwide.
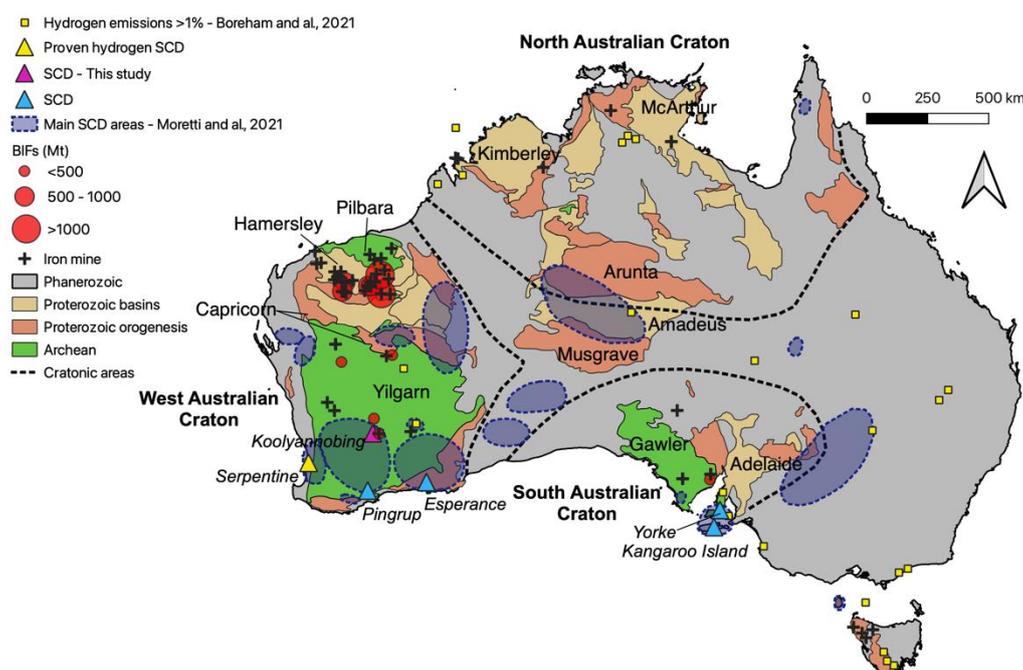
Figure 2. Simplified geological map of Australia and locations of the study areas from previous authors [12,27] and in this paper. Pink triangles represent the SCD areas and the studied BIF are from Hamersley.

The presence of H_2 in wells have been noticed in Australia for almost one century [31,32]. More recently, numerous SCD have been noticed in Western and Central Australia, probably indicating H_2 seepage [12,26]. These depressions are occurring at the top of sedimentary layers and span all over Precambrian cratons, as shown in blue in Figure 2. A previous study consisted in mapping hundreds of circular structures on five different locations (Serpentine Area (Perth Basin), Pingrup Area, Esperance Area, Yorke Peninsula, Kangaroo Island) [12] in order to compare them to areas of proven H_2 emanations such as Russia and Brazil [9,25]. Lately, field acquisitions in the Yilgarn Craton confirmed H_2 emissions above SCD in the Perth area, hence proving that the proxy is relevant [27]. In addition, H_2 has been sampled in the Frog's Leg Gold mine of the Yilgarn Craton as well as CH_4, likely due to H_2/CO_2 interaction according to the isotope data [33].

2.2. South Africa

South Africa has a long and complex geological history. A structural sketch is presented in Figure 3. The north-eastern part is constituted of an Archean basement, the Kaapvaal Craton, dated back to Eoarchean with estimated ages of 3600 My [34]. The rocks consist mainly in granite, greenstone belts and metamorphic rocks. This basement is sometimes outcropping or could be capped by younger Proterozoic layers, made up of dolomite, conglomerate, silt quartzite and banded irons formations and sometimes intercalated by basic volcanic events. This sedimentary series is subdivided into three super groups: Witwatersrand, Ventersdorp and Transvaal. In the Bushveld District, a large basic intrusive complex is known to have set up around 2060 My [35] and is considered to be one of the richest mineral deposits on the planet in terms of the platinum group metals. In the south, the E-W Namaqua-Natal Belt surrounds the Kaapvaal Craton. It is a Proterozoic terrane accreted to the Kalahari Craton at around 1200 My [36]. It is now capped for its major part by Phanerozoic sedimentary rocks of the Karoo Supergroup but still outcrops in the western part of the country. Finally, the Karoo Gp, dated from Carboniferous to Jurassic, are spread over a large part of the country and largely cover the Namaqua-Natal Belt and the southern part of the Kaapvaal Craton. These rocks are essentially detrital. Nowadays, iron is largely exploited in South Africa, where Fe-rich lithologies are outcrop-

ping. Iron mines are mainly located in Archean and Proterozoic terranes, in areas where BIF are numerous.
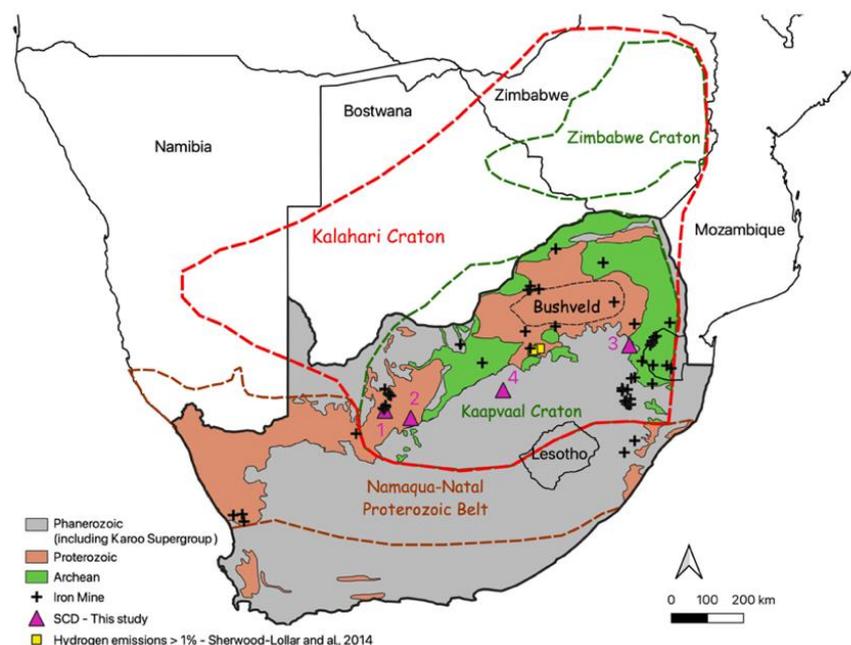
Figure 3. Simplified geological map of South Africa and locations of the study areas in purple. Zone 1 corresponds to Kolomela BIF-hosted iron mine.

For now, no work has been yet dedicated to explore H_2-emitting SCD in South Africa, but few works already pointed out the presence of H_2 emissions in South Africa, located within Proterozoic terranes and near iron mines [11].

2.3. Brazil

The São Francisco Basin is one of the several Proterozoic basins in Brazil (Figure 4). It is N–S oriented, bounded by two orogenic belts and corresponds to a double foreland basin with the Brasilia Belt westward and the Araçuai Belt eastward. Both were created during the Brazilian Orogeny, at the end of the Proterozoic. The stratigraphic column in the São Francisco Basin includes rocks from Archean metamorphic basement (>1800 My) that can reach up to 7 km in thickness and ends with the Neoproterozoic Tres Maria Formation (576 Ma) of the Bambui Group [37]. The region is rich in BIF, and many iron ore mines are active particularly in the Quadrilatero Ferrifero. These BIF, while not outcropping, are also very likely present underground, since large magnetic anomalies have been recognized near the area where H_2 is naturally escaping [37].

Hundreds of SCD have been observed and mapped in this basin, and some of them have already been monitored, displaying H_2 emissions overpassing 600 kg/day/structure (zone 1, 2 and 3 in Figure 4) [9,13].
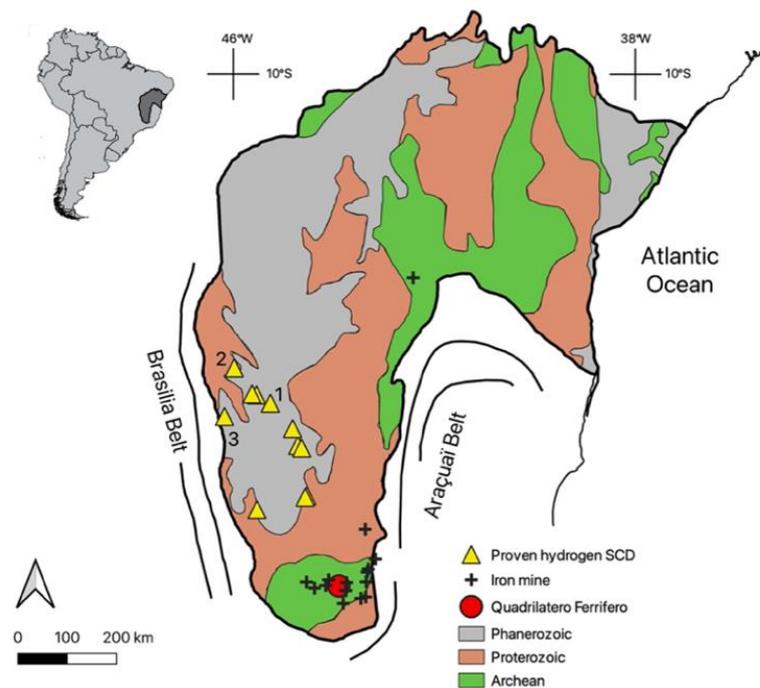
Figure 4. Simplified geological map of the São Francisco Basin and locations of the study areas. The 1, 2 and 3 sites hosting proven hydrogen-related depressions have been published by [9,13]. The other ones are unpublished data.

2.4. BIF and Relationship between These 3 Cratonic Areas

The three cratonic areas correspond to old Precambrian rocks (São Francisco in Brazil, Kaapvaal in South Africa and Pilbara and Yilgarn in Western Australia) preserved from tectonics through the ages and host in consequence massive BIF. Fresh BIF from these three areas exhibit a standard Precambrian BIF chemistry with SiO_2 from 34 to 56 wt% and total Fe content from 20 to 40 wt% with Fe^{3+}/Fe_{tot} ranging from 0.05 to 0.58. Minor elements such as CaO and MgO are found below 10 wt%, while MnO or Al_2O_3 are found below 2 wt%. The minerals found are mainly quartz, Fe oxides (magnetite and hematite), Fe silicates (riebeckite, greenalite, stilpnomelane) and Fe carbonates (siderite, ankerite), with a variability depending on the starting bulk chemical composition and the metamorphism undergone [22]. Sometimes, BIF have been enriched by low temperature processes involving the oxidation of Fe^{2+} into Fe^{3+} and hydration with total Fe content around 58–65 wt% for Australian BIF-hosted iron ores [21,38]. The primary minerals such as magnetite are martitised (oxidized into hematite) and carbonate, silicates and quartz are replaced by goethite. In the literature, this oxidative mechanism of BIF reaching the surface has been identified for long ([16] and references therein), but it is not known if it has been accompanied by H_2 generation.

3. Rounded Depressions in BIF Rich Areas

3.1. Rounded Depressions Related to Gas Escape

Previous works have emphasized the similarities between the size, expressed in equivalent diameters, the size distribution and the depth/diameter ratios of the P_H$_2$_SCD worldwide. The distributions are usually unimodal, with mean equivalent diameters ranging from tens to few hundreds of meters, respectively 276, 302 and 178 m on average in the three studied zones in Brazil and 262 m in Russia [12]. In all these areas, the presence of H_2 is proven and has been measured by gas detectors. The depth/diameter ratio has been established to be a major characteristic of P_H$_2$_SCD, always falling around 1% [12]. The slope of these depressions is also a characteristic that allows to discriminate them from dolines, usually displaying, at least locally, high slopes over $20°$ [12].

Some of the SCD mapped in this work in the vicinity of the BIF-hosted iron mines are presented Figure 5 together with P_H₂_SCD from Brazil and Western Australia.
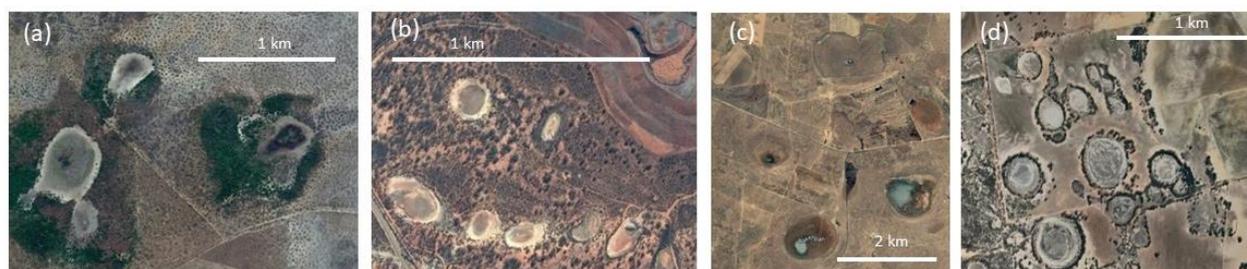

Figure 5. Sub-Circular Depression observed from aerial photographs. (**a**) In the Mina Gerais in Brazil, H_2 values in the soil could be found in [9,13]. (**b**) Near the Koolyanobbing BIF mines in Australia, the border of the mine is visible in the upper-right corner; see location Figure 2. (**c**) SCD in South Africa, area n°4, see location Figure 3. (**d**) P_H₂_SCD northward from Perth; H_2 contents have been published by [27].

In the literature, topographic depressions in the landscape have already been mentioned above BIF layers. Authors have explained it by the leaching-induced dissolution of mobile elements in BIF creating underground cavities that make the soil above collapse [39]. These related depressions are highly irregular in shape and hence do not match with the rounded features presented in this work, making them unlikely to be related to such collapsing phenomenon. Nonetheless, a statistical study on their morphology might help to determine whether they are likely H_2-emitting SCD.

3.2. Presence of SCD around the BIF Mines

SCD are now recognized as a good proxy for natural H_2 exploration. Using the presence of iron mines and especially BIF-hosted iron mines as an indication of potential H_2 generation sites, aerial photos from South Africa and Western Australia were analyzed. These two regions, as well as the São Francisco Basin in Brazil, which had been previously studied, show an apparent spatial correlation between BIF and the rounded features. In Australia we explore a new site (Australia_1) located within the Archean Yilgarn craton in Western Australia (Figure 2), rich in SCDs that directly surround the operating Koolyanobbing BIF-hosted iron mine, as shown in Figure 6. In South-Africa, we analyze four sites of interest from the Kaapvaal Craton (see 1, 2, 3, 4 in Figure 3), exhibiting sub-circular structures in the vicinity of operating BIF-hosted iron mines. The first site (South_Africa_1) is directly located tens of meters away from the Kolomela mine, as shown in Figure 7. The second and the third ones (South_Africa_2 and South_Africa_3) are located tens of kilometers away from active BIF-hosted iron mines. The fourth one (South_Africa_4) is located on top of the Phanerozoic sedimentary layer, a hundred kilometers away from the closer active BIF-hosted iron mine, but the presence of BIF below the sedimentary layers is possible.

Finally, in Brazil, we focus on the rounded structures that displayed H_2 emissions in previous studies (see 1, 2 and 3 in Figure 4). They are located few hundreds of kilometers away from the outcropping BIF of the Quadrilatero Ferrifero. However, as suggested by the magnetic anomaly described in the vicinity of the P_H₂_SCD [37,40], the presence of buried BIF below the P_H₂_SCD should not be disregarded.
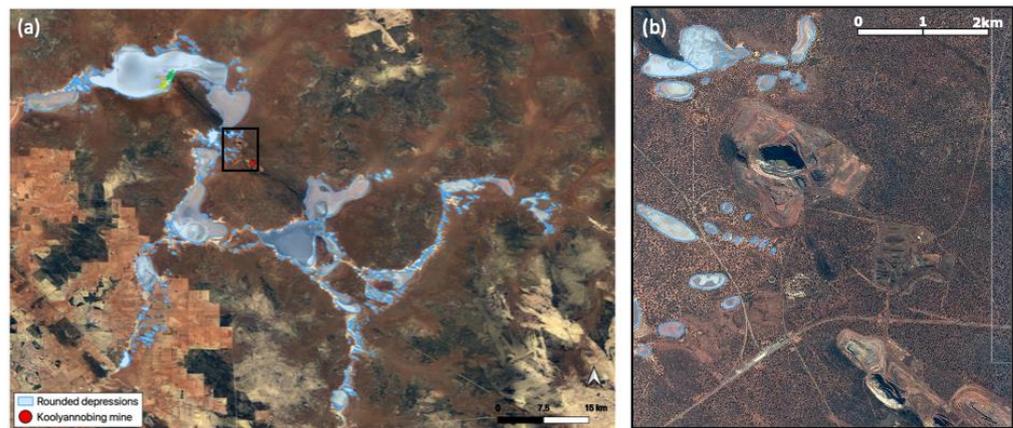
Figure 6. (**a**) Aerial photo of Koolyanobbing mine (Australia, see location Figure 2) and its SCD high-lighted in blue. (**b**) Zoom on the black rectangle in (**a**), showing SCD located around the mine pits.
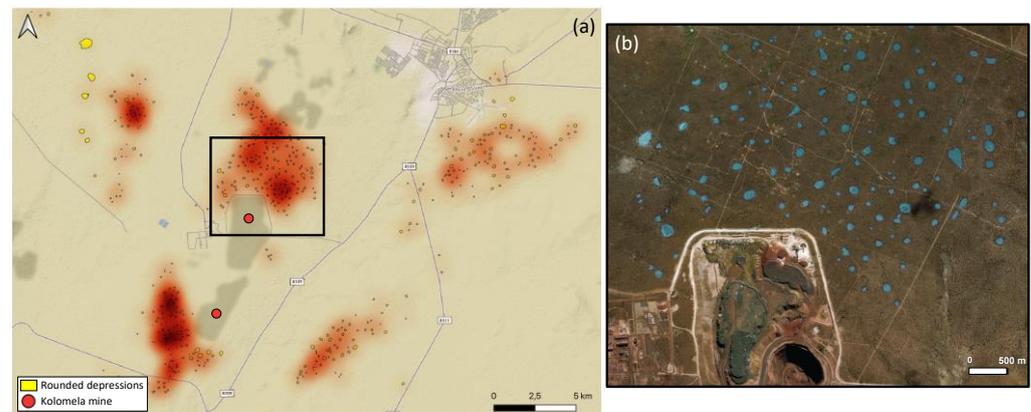

Figure 7. (**a**) SCD mapped (in yellow) in the South_Africa_1 zone in the vicinity of the Kolomela mine (see location Figure 4). The intensity of the reddish color corresponds to the number of depressions per surface unit. The grayish spots are the pits and other human facilities. (**b**) Zoom in on the Kolomela mine and its surroundings with SCD highlighted in blue.

3.3. Statistics on SCD around BIF Mines in Australia and South Africa

As previously stated, the statistics on the H_2 emitting structures have emphasized the similarities between the size, the size distribution and the depth of the P_H_2_SCD worldwide [12]. The SCD areas recognized by this proxy in Western Australia has then been proven to emit H_2 [27], so the same analyses have been carried out for the five new areas from South Africa and Australia where BIF are outcropping or suspected in the subsurface. The characteristics of each area are reported in Table 1 and Figure 8.

Table 1. Characteristics of the five new mapped areas in South Africa and Australia.

SCD	South_Africa_1	South_Africa_2	South_Africa_3	South_Africa_4	Australia_1
Nb of mapped structures	624	792	866	486	612
Min. equiv. diameter (m)	8	19	22	35	45
Max. equiv. diameter (m)	437	856	2961	2633	12,784
Mean equiv. diameter (m)	67	98	346	476	407
Median equiv. diameter (m)	59	88	187	412	200
Depth/diameter	0.017	0.019	0.005	0.014	0.013
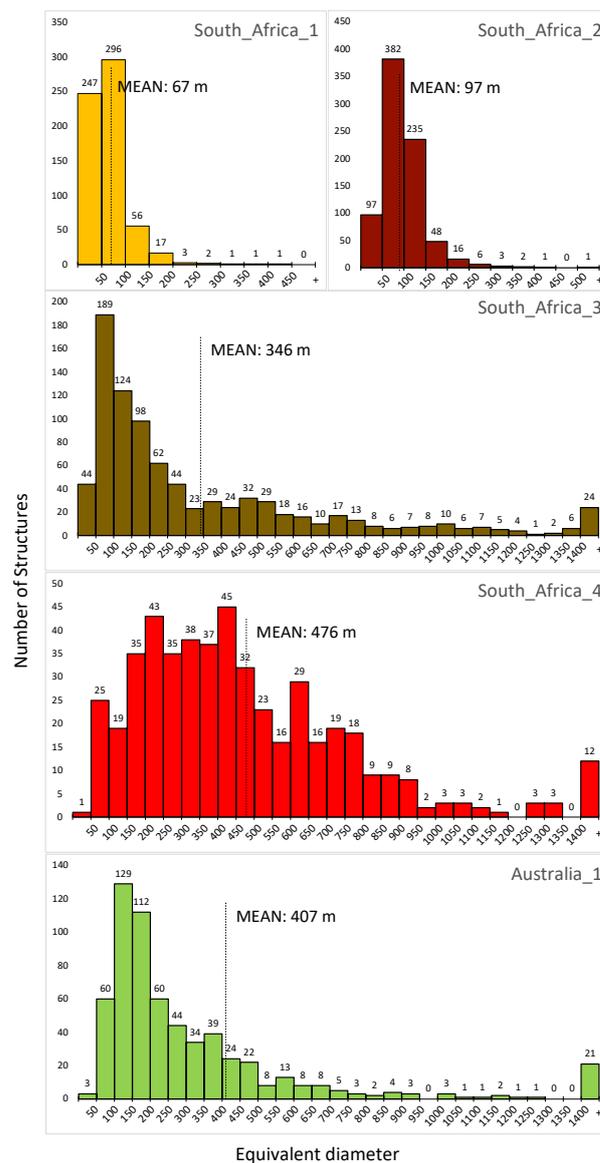
Figure 8. Size distribution of the SCD expressed as equivalent diameter (m) for five new areas in South Africa and Australia.

The distribution of feature sizes expressed in the equivalent diameter is provided in Figure 8. Except for South_Africa_1 and South_Africa_2, it is interesting to point out that median equivalent diameter values are far from mean equivalent diameter values. It can be explained by the high number of features exceeding 1400 m of equivalent diameter for these three areas (24 for South_Africa_3; 12 for South_Africa_4; 21 for Australia_1) that increase the mean diameter. This might reflect the merging of several depressions with time.

3.4. Comparison with the SCD Distributions of the São Francisco Basin

3.4.1. SCD Sizes

The size distribution of the mapped depressions in Australia and South Africa is compared in Figure 9 with the Brazilian depressions where H_2 has already been detected. For a better comparison, the size distribution of each area has been normalized to the class presenting the higher number of features. The Figure shows that many areas in different regions exhibit a very similar pattern (South_Africa_1, South_Africa_2, South_Africa_3, Australia_1 and Brazil_3) with a unimodal distribution and a rather small modal size (0–200 m equivalent diameter), even if the dispersion can vary from one to another area.

On the contrary, three other sites (South_Africa_4, Brazil_1 and Brazil_2) show a larger spectrum of size distributions. Brazil_1 and Brazil_2 exhibit a barely unimodal distribution with much higher sizes and dispersion, while South_Africa_4 shows a large spectrum but almost no small structures.
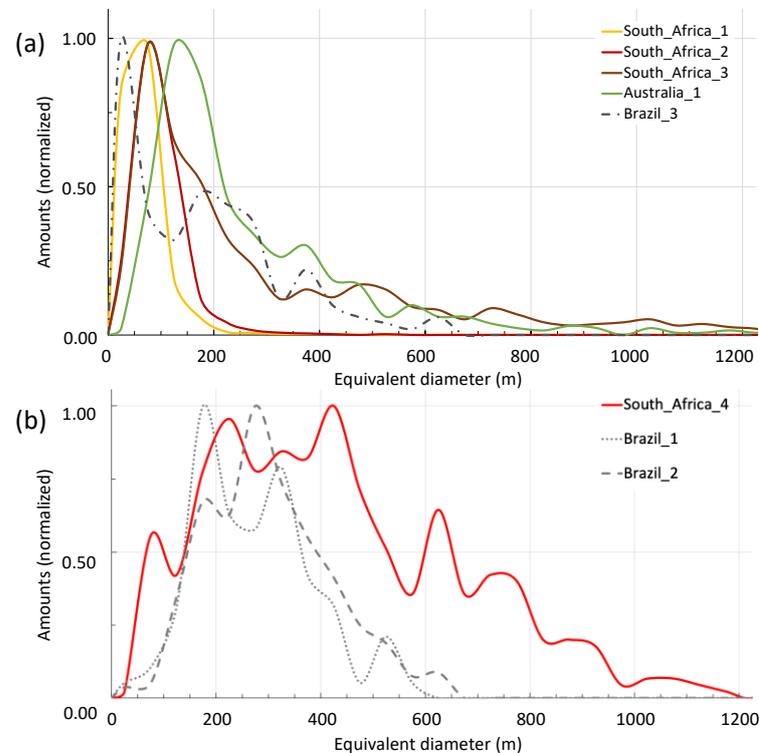
Figure 9. Comparison of normalized size distribution of the mapped depressions from South Africa and Australia with the proven zones of H_2 emissions in São Francisco, Brazil. (**a**) Distributions with similar unimodal distribution: a small median and average value around 100 m. (**b**) Distributions with larger spectrum and mean values above 200 m.

From these graphs, it is tempting to consider the unimodal distribution as a characteristic pattern and the range 0–200 m as the characteristic equivalent diameter size of the SCD, while the wider distributions around larger average values might correspond to a set of initial and merged depressions explaining the high variability in features sizes. Brazil_1, which exhibits an intermediate pattern, might be a transitionary stage.

The relationship between the depth of the H_2 generation and the size of the SCD is not direct, as it also depends on many parameters, such as the micro-organism activity (that consumes the H_2) or the relative permeability of the soil (that influences the speed of the transport toward the surface) [24]. Nonetheless, knowing that South_Africa_1, South_Africa_2, South_Africa_3 and Australia_1 are located very close to iron mines, we consider the unimodal distribution as well as the range 0–200 m of equivalent diameter as a characteristic pattern for SCD originated from a shallow depth H_2 and spread out generation zone, matching with water–BIF interactions. At the same time, the uncertain patterns with the high variability of South_Africa_4, Brazil_1 and Brazil_2, located further to the mines, might correspond to merged fairy circles originating from deeper H_2 generation that complexify the signal at the surface. However, the dynamics of H_2 migration upward in Australia and South Africa have to be further studied, as it has been realized in São Francisco with the characterization of microorganisms [23] that consume the H_2.

3.4.2. SCD Depths

It has been noted on the previous studies of P_H_2_SCD that the morphology of the depression, size/depth ratio and slope may help to discriminate them from dolines and

other depressions related to karst systems [12]. In Brazil and Russia, this ratio was around 1%. Figure 10 shows very similar ratios for the five new studied zones in South Africa and Australia, with ratios between the depth and equivalent diameters between 0.5% and 2%. This result infers probable H_2 emissions at these SCD, which need now to be monitored in-situ.
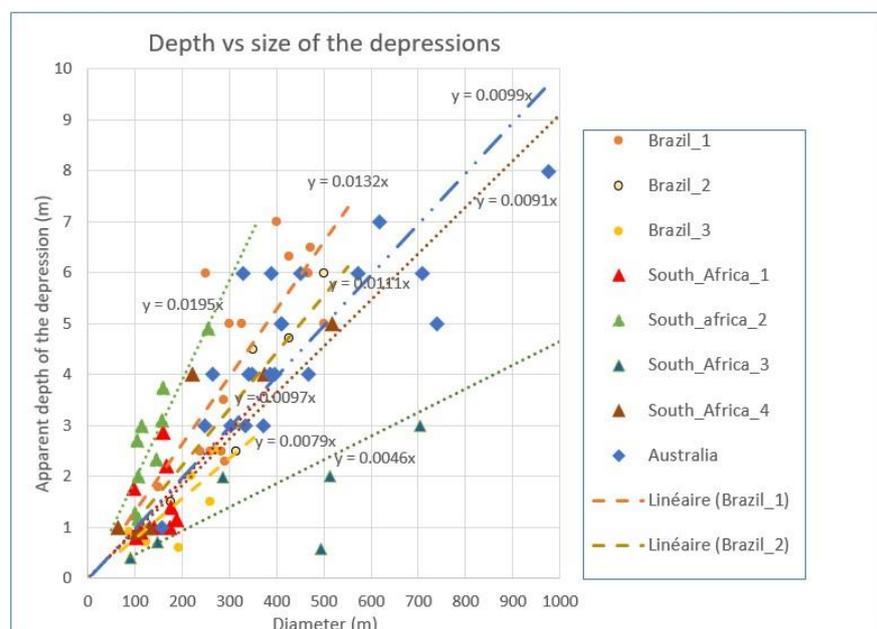
Figure 10. Depth/diameter ratio for SCD from Brazil, South Africa and Australia. Brazilian data from [12], see location Figure 4. Australian and South African data are from this study; see location of the mapped areas on Figures 2 and 3.

## 4. BIF Potential for H_2 Production: Case Study of Australian Samples

4.1. Geological Context and Sampling

We showed the presence of sub-circular depressions in the vicinity of BIF-hosted iron mines, inferring that BIF could be involved in H_2 generation. As fresh BIF-host important quantities of ferrous iron (Fe_{tot} from 20 to 40 wt% and Fe^{3+}/Fe_{tot} from 0.05 to 0.58) [22], they can indeed theoretically produce H_2 by oxidation via water alteration. These undirect elements need to be further investigated and the relationship between BIF and H_2 constrained unambiguously.

A petrological study was conducted on natural samples coming from Hamersley Province in Western Australia (Figure 2). The Hamersley Group is a Precambrian (2600–2450 My) marine deposit of 2.5 km thickness lying horizontally or with a northward low dip, over 40,000 km^2 in the Pilbara Craton. It is divided into eight formations consisting in BIF, shales, carbonates and volcanics [41]. Among these formations, the Brockman Formation constitutes the major iron ore reserve, especially the Dales Gorge Member, which is mined in areas such as in Mt Tom Price (22.75° S, 117.77° E). For the Dales Gorge Member, studies conducted on fresh BIF revealed low greenschist facies metamorphism throughout the province and a lateral continuity in chemical composition as well as microbands and macrobands thicknesses [42]. Mineral analyses highlighted the presence of ferrous BIF minerals corresponding to low-grade metamorphism [22]. In the Dales Gorge Member, siderite is the main carbonates, while stilpnomelane and minnesotaite are the major silicates [42,43].

For this study, three samples were selected in the Hamersley Province (Figure 2) and are presented in Figure 11. One fresh sample (hereafter referred as BIF1) was selected from a diamond core from the Dales Gorge Member (Brockman Formation) at a depth of 100 m near Mt Tom Price. It is approximately 15 cm high and constituted of alternate bands of similar thickness, around 2–3 cm. In the lower part, they are light red (B1A) and dark red

(B1B), while on the upper part the bands are dark grey (B1C) and light grey (B1D). At a macroscale, some bands appear heterogeneous and exhibit alternates of sub-millimetric levels, such as the B1A band. The sample is highly cohesive and does not show massive surficial alteration features, which is in agreement with the depth of sampling. Two other samples (BIF2 et BIF3) were sampled at the surface near Newman, from Bruno's Band (Sylvia Formation) and Dales Gorge member, respectively. The BIF2 size is approximately 15 cm, and the banding is more complex than on BIF1. On the lower part (B2B), the bands of variable sizes, from few millimeters to 1 cm, are white and grey-reddish, with even smaller grey-reddish levels slightly visible in some white bands. At band interfaces, the reddish color is often reinforced. On the upper part (B2A), the sample turns into orange, and the banding becomes hardly visible. The BIF3 is approximately 20 cm high. In the lower part (B3C), the banding is very expressed with alternate bands of dark grey and white color, ranging from a few millimeters to 1 cm. In the medium and upper parts (B3B and B3A), the banding is essentially made up of sub-millimetric with minor millimetric or centimetric levels. Although some bands still are whitish or dark grey, the dominant color is orange. BIF2 and BIF3 samples are more friable and brittle. We also observe an orange color zonation from the bottom to the top of the samples, suggesting a surficial alteration.
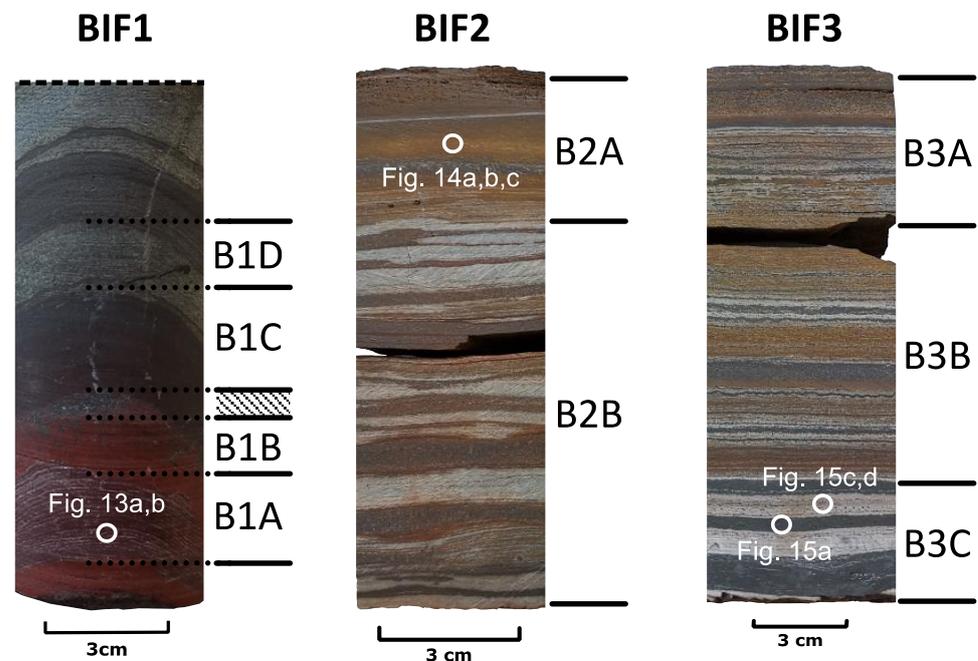
Figure 11. Studied samples from Hamersley Province, Western Australia. They are segmented in different zones. The names on the right of the samples correspond to the powders analyzed. White circles correspond to microscopic observations presented in Figures 13–15.

4.2. Methods

Sample preparation—To represent the variability within the rock, samples were segmented in different zones mainly on the criteria of color and homogeneity. Then, the samples from each zone were manually powdered in an agate mortar and sieved to obtain a grain size below 100 μm. Two sub-samples per zone were produced to undertake mineral and chemical characterization. In parallel, thin sections (30 μm thick) crossing each zone of interest were also made (LMV, Clermont-Ferrand) for a petrographic study at the microscopic scale.

X-ray diffraction—Mineralogical compositions of the powders were obtained by conducting X-ray diffraction analysis using a D2 Phaser from Brucker (LFCR, Pau). The CuKα radiation at 30 kV and 10 mA and the SSD160 detector were used. A time step of 0.2 s counting time per step and a 0.02 2θ step between 5 and 80° with 30 trs/min were used for measurements.

Optical Emission Spectroscopy by Inductively Coupled Plasma (ICP-OES)—Analyses of bulk compositions through major and minor element contents were conducted on the powders by the SARM (CRPG, Nancy), using ICP-OES on an iCap 6500 (ThermoFischer Scientific). It must be noted that the Fe content is expressed as Fe_2O_3, even if samples contain Fe^{2+}. Considering the high levels of SiO_2 and Fe_2O_3 in the samples, the given uncertainty for these components is lower than 2 wt%. As far as the minor elements are concerned (Al_2O_3, MnO, MgO, CaO, Na_2O, K_2O, TiO_2 et P_2O_5), the given uncertainty is between 10 and 20%. The volatile content in the sample is given by the loss on ignition. Each analysis was repeated twice.

^{57}Fe Mössbauer spectroscopy—To complete the ICP-OES analyses and determine iron speciation in the samples, 500 μg of each powder was analyzed with a constant acceleration Halder-type spectrometer (ICMCB, Bordeaux) equipped with a ^{57}Co radioactive source (embedded in a Rh matrix), which was maintained at 293 K. The spectrometer was calibrated using a pure α-Fe0 foil as an external reference. All spectra were recorded in transmission geometry at ambient temperature. The Mössbauer hyperfine parameters and the relative areas of each component were refined with the WinNormos software (Wissenschaftliche Elektronik GmbH). Two analyses were made per powder, and each analysis lasted about 1 day. The given uncertainty is 3%.

Optical and electron microscopy—An optical study was performed using a Nikon Eclipse LV10ND microscope. The nature of the samples (rich in opaque iron oxides) required a work under both transmitted and reflected lights. Scanning electron microscopy (SEM) was also performed on the thin sections coated with 20 nm of carbon, using the SEM ZEISS Supra 55 VP (ISTeP, Paris, France). Imaging was realized using an electron beam at 15 keV and an AsB detector. Some EDS spectra were also acquired to get the semi-quantitative chemical composition of the phases.

4.3. Results

4.3.1. Samples Composition

- Iron content and speciation

Iron content and speciation results are provided in Table 2. All Mössbauer and ICP-OES data are available in Appendices A and B. For the fresh sample (BIF1), the different bands that have been analyzed exhibit similar total Fe content ranging from 11.78 wt% (B1A) to 15.12 wt% (B1B), except for one band that carries much more total Fe with 56.83 wt% (B1C). This high variability is characteristic of BIF facies with iron quartz rich bands and iron oxide rich bands. Iron occurs in both oxides/oxi-hydroxide and silicate minerals. Fe^{3+} is always carried by iron oxides/oxi-hydroxides, mainly hematite between 30% (B1D) and 76% (B1B) and magnetite ($Fe^{3+}_{tetrahedral}$ + 1/2 $Fe^{2+/3+}_{octahedral}$) between approximately 10% (B1B) and 44% (B1C). Fe^{2+} is carried by oxides and silicates to a lesser extent, with Fe^{2+} content in magnetite (1/2 $Fe^{2+/3+}_{octahedral}$) and silicates reaching, respectively, 20% (B1C) and 6% (B1A) of Fe_{tot}. It is interesting to note that Fe-silicates have only been detected in B1A, B1B and B1D: the quartz rich bands (where total Fe content is lower). This can be explained by the very high content of iron oxide in B1C that hide the Fe-silicate signal during Mössbauer analyses. Because many Fe^{2+} silicates have similar Mössbauer parameters, the nature of Fe^{2+} silicates in B1A, B1B and B1D cannot be determined unambiguously, even more if it consists in a mix of different silicate species. Nonetheless, Mössbauer parameters for Fe^{2+} silicates in this samples match Mössbauer parameters of both stilpnomelane and minnesotaite [43,44]. Finally, the calculated Fe^{3+}/Fe_{tot} ratios are high in this sample and exhibit a bimodal variability with B1A and B1B ratios of 0.90 and 0.96, respectively, whereas B1C and B1D ratios are 0.81 and 0.79. This bimodal variability with a higher oxidation in B1A and B1B matches the preferential presence of Fe^{3+}-hydroxides (ferrihydrite, goethite, lepidocrocite) in these bands as well as the reddish color of the lower part of the BIF1 sample (Figure 11), inferring an oxidation episode by water circulation in some bands of this sample.

Table 2. Iron content and speciation in BIF1, BIF2 and BIF3 samples.

| Sample	Iron Speciation—Mössbauer Spectroscopy (%)								Iron Content ICP-OES (wt%)
	Hematite	Goethite *	Ferrihydrite	Magnetite		Silicate			
	Fe^{3+}	Fe^{3+}	Fe^{3+}	Fe^{3+}_{tetra}	$Fe^{2+/3+}_{octa}$	Fe^{3+}	Fe^{2+}	Fe^{3+}/Fe_{tot}	Fe_{tot}
B1A	43	10	23	10	8	N.D.	6	0.90	11.78
B1B	76	10	N.D.	6	7	N.D.	<3	0.96	15.12
B1C	34	N.D.	3	24	39	N.D.	N.D.	0.81	56.83
B1D	30	N.D.	13	19	33	N.D.	5	0.79	14.08
B2A	18	78	N.D.	<3	<3	<3	N.D.	1.00	42.57
B2B	35	56	N.D.	4	3	<3	N.D.	0.99	28.95
B3A	18	50	N.D.	14	13	5	N.D.	0.94	27.01
B3B	13	43	N.D.	18	19	7	N.D.	0.91	36.87
B3C	56	N.D.	N.D.	25	19	N.D.	N.D.	0.91	41.70

* goethite (α-FeOOH) + lepidocrocite (γ-FeOOH). N.D.: Not Detected.

For the altered samples (BIF2 and BIF3), the total Fe content is much higher than BIF1 ranging from 27.01 wt% (B3A) to 42.57 wt% (B2A). Although BIF2 and BIF3 have been segmented in different zones containing several quartz-rich and iron oxide-rich bands that average the mean compositions of the zones, the higher total Fe content in these altered samples is essentially significative of iron enrichment by water circulation in subsurface conditions. For BIF2 and BIF3, Fe^{3+} is carried predominantly by oxides/oxi-hydroxides like in BIF1. Goethite is the main Fe^{3+}-bearing mineral ranging from 43% (B3B) to 78% (B2A) of Fe_{tot}, highlighting the high rate of hydration and alteration of the samples, except for B3C where hematite is predominant. On the contrary to BIF1, the little amount of iron contained in silicates is exclusively Fe^{3+}. Finally, the low amount of Fe^{2+} is totally carried by magnetite (1/2 $Fe^{2+/3+}_{octahedral}$), with content evaluated from <2% (B2B) to 10% (B3C/B3B). The calculated Fe^{3+}/Fe_{tot} ratios for these samples are even higher than for the BIF1, from 0.91 (B3C/B3B) to 1.00 (B2A).

- Mineralogy

For the Fresh BIF sample (BIF1), quartz is always abundant, even if it is less present in B1C (Figure 12). Iron oxides are also present in high contents, consisting in dominant Fe^{3+} oxide (hematite) and to a lesser extent Fe^{2+}/Fe^{3+} oxide (magnetite), except for B1C where magnetite is dominant (Figure 12). No Fe^{3+} oxi-hydroxide (goethite) is detected in this sample. Finally, it is interesting to point out the detection of low content phases in the B1A and B1B strips. Indeed, calcite is clearly visible in B1B, while riebeckite is slightly detected in B1A with characteristic peaks at $2\theta \approx 10.5°$ and $28°$. The XRD observation of riebeckite, a Na-amphibole-bearing Fe^{2+}, in low a content in this sample is consistent with Mössbauer results that revealed the presence of Fe^{2+} carried in low amounts by silicates that might be riebeckite. The riebeckite presence in this sample coming from Dales Gorge Member is also consistent with previous studies, as riebeckite was determined to be a ubiquitous mineral of this member [42].

For the altered samples (BIF2 and BIF3), the mineralogy consists exclusively in quartz and iron oxides/oxy-hydroxide (Figure 12). BIF2 and BIF3 exhibit a high content of Fe^{3+} oxy-hydroxides (goethite), except for B3C. Fe^{3+} oxide (hematite) is also highly present in these samples. Fe^{2+}/Fe^{3+} oxide (magnetite) is also detected but in amount much lower than Fe^{3+} oxide/, except for B3C where magnetite is still strongly present. Finally, neither carbonate nor Fe^{2+} silicate have been detected by XRD analyses in the altered samples, implying very low concentrations (under a few percent) if present. These results are significant of a higher oxidation degree of BIF2 and BIF3 compared to BIF1 and are in good agreement with higher Fe^{3+}/Fe_{tot} ratios of BIF2 and BIF3 than BIF1 (Table 2).
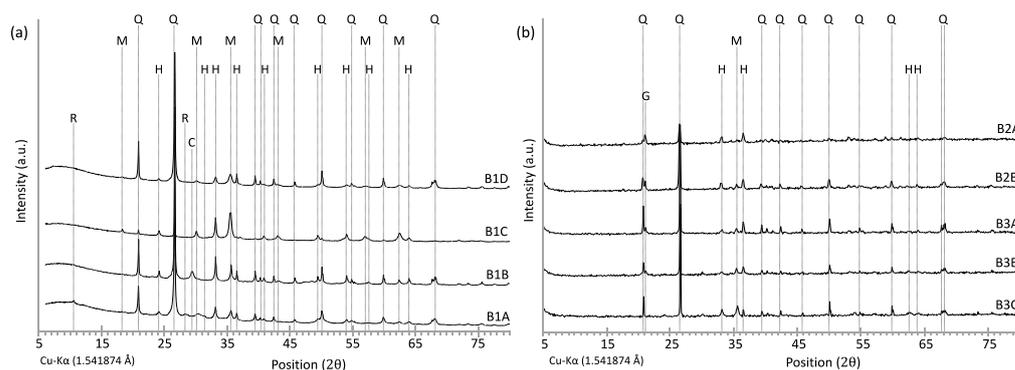
Figure 12. XRD patterns obtained and interpreted for (**a**) the fresh BIF sample (BIF1) and (**b**) the altered BIF samples (BIF2 and BIF3). Letter Q refers to quartz, M to magnetite, H to hematite, G to goethite, R to riebeckite and C to calcite.

### 4.3.2. Microscopic Observations

- Fresh BIF

The petrographic study conducted at a microscopic scale on the fresh sample by SEM revealed a highly characteristic textural assemblage present in the whole B1A strip. As shown in Figure 13, small and rounded minerals were noticed in bright white, forming little clusters of a few micrometers. A punctual semi-quantitative analysis performed on these minerals showed that they correspond to iron oxide (Figure 13c). Fibrous minerals of tens/hundreds of centimeters in light gray color were also observed in a matrix of quartz in dark gray. The observation of such asbestos texture is consistent with the presence of silicate detected during Mössbauer analyses. A punctual semi-quantitative analysis performed on these fibrous minerals confirmed that they correspond to iron silicate (Figure 13d). Although XRD analyses revealed the presence of riebeckite (Na-amphibole) in the samples, the composition of the Fe^{2+} silicate herein includes Fe, Mg, K, Al, Si and O but lacks Na and thus demonstrates that several asbestos Fe^{2+} silicates are present in the sample. The qualitative composition provided here matches the theoretical composition of minnesotaite $((Fe^{2+}, Mg)_3Si_4O_{10}(OH)_2)$, as well as Mössbauer results and common minerals found in the Dales Gorge Member [42].

As presented in Figure 14, the BIF2 exhibits alternating microbands of highly reflective hematite and less reflective goethitic fibrous minerals in a matrix of quartz. The Figure 14b shows fibrous goethite in the matrix of quartz under transmitted light, appearing red-brownish when not extinct.

The BIF3 corresponds at macroscale (Figure 10) to dark and bright strips. This pattern is also observed at the microscale with Fe oxide-rich layers alternating (Figure 15a) with quartz layers (Figure 15c,d). Under reflected light, the white-pinkish euhedral iron oxides are stripped by even whiter straight lines (Figure 15a). In this sample, goethite is also observed surrounding the euhedral oxide minerals (light gray color in Figure 14a) or into veins in the quartz levels (red-brownish color in Figure 15c). Finally, the quartz levels contain minor euhedral oxide minerals, almost fully destabilized and crosscut by goethite veins (Figure 15d).
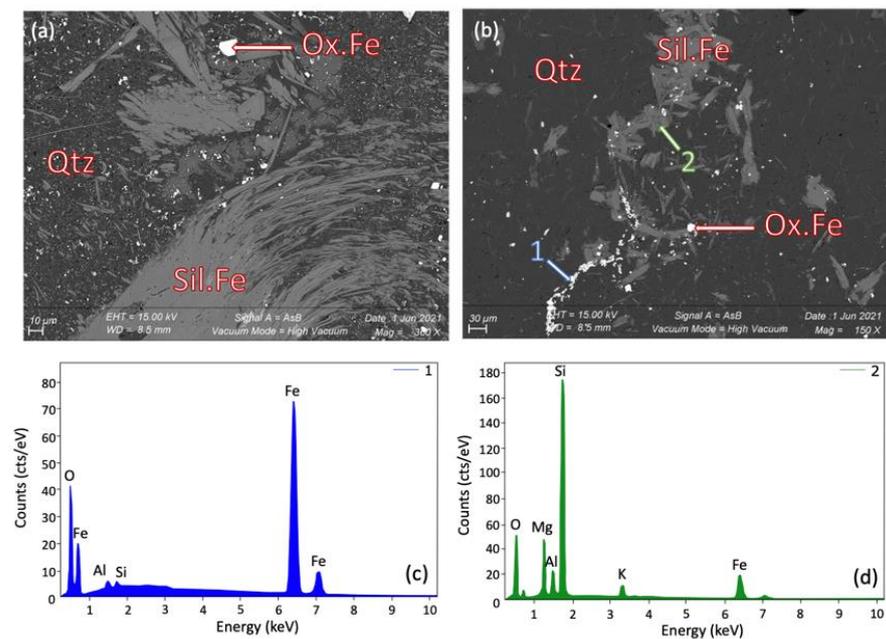
Figure 13. (**a**,**b**) Fibrous silicates observed by SEM in the fresh BIF sample (BIF1). Qtz corresponds to quartz, Sil.Fe corresponds to iron silicate and Ox.Fe corresponds to iron oxide. (**c**,**d**) Spectra of punctual semi-quantitative analyses performed on the two points located on image (**b**). (**c**) Iron oxide, point 1. (**d**) Iron silicate, presumably minnesotaite, point 2.
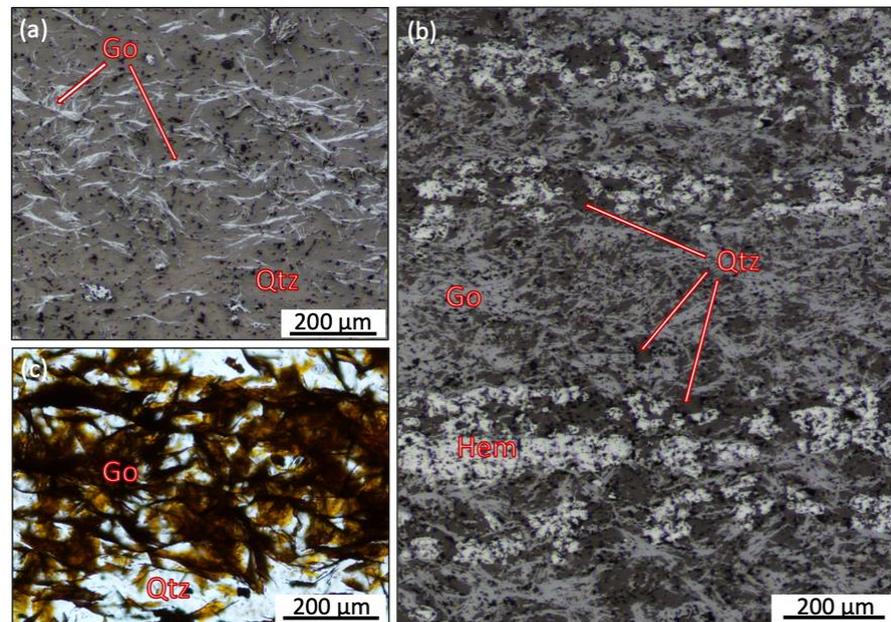
Figure 14. Altered BIF2 sample observed by optical microscopy under (**a**,**b**) reflected and (**c**) transmitted lights. We observe fibrous goethite between quartz grains. See location on Figure 11.
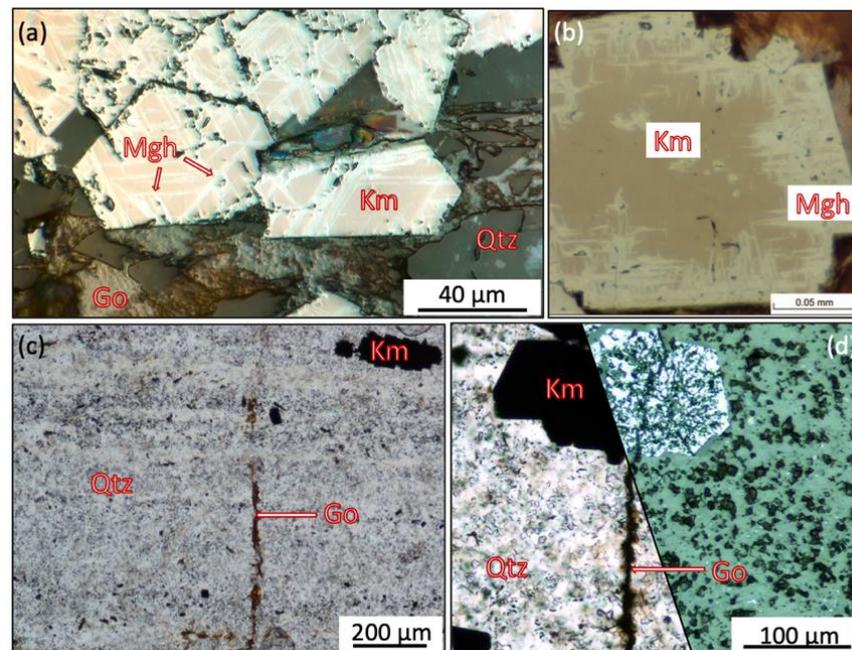
Figure 15. Altered BIF3 sample observed by optical microscopy under (**a**,**d**) reflected and (**c**,**d**) transmitted lights. (**a**) Typical texture of iron oxide-rich levels. (**c**,**d**) Typical textures observed in quartz-rich levels. See location on Figure 11. Image (**b**) is extracted and modified from [45].

4.4. Discussion

4.4.1. Mineralogical Evidence for H_2 Production

- Fe^{2+}-bearing silicates alteration

Ferrous iron in fresh BIF can occur as silicates (ex: greenalite $Fe^{2+}_6Si_4O_{10}(OH)_8$) or carbonates (ex: siderite $Fe^{2+}CO_3$) [22]. As the oxidation of iron in the samples is high, as indicated by high Fe^{3+}/Fe_{tot} ratios (0.79 to 1), the presence of ferrous phases is limited.

XRD analyses only showed small amounts of remanent riebeckite, a Na and Fe^{2+}-bearing amphibole for one strip of the least-altered sample (B1A). The Mössbauer spectroscopy, which exclusively focuses on the iron speciation and its mineralogy, provides complementary results to XRD albeit with a lower detection limit. Mössbauer results indicated that Fe^{2+}-bearing silicates are still present in several strips of the least-altered sample (B1A, B1B, B1D) such as riebeckite or minnesotaite, whereas the more altered samples show Fe^{3+}-bearing silicates. Microscopic observations of the least oxidized sample (BIF1) indeed confirmed the presence of fibrous Fe^{2+}-silicates, presumably riebeckite and/or minnesotaite (Figure 13), while a more oxidized sample (BIF2) showed needle-shaped goethite (Figure 14). A comparison between these two BIF highlights the morphological similarities between the iron silicates in the least oxidized sample and the iron oxi-hydroxide (goethite) in the more oxidized one. This observation suggests the replacement in-situ (pseudomorph) of primary iron minerals, in this case the silicates, by secondary goethite during the surficial alteration and hydration. This phenomenon is considered in the literature as a marker of BIF ore formation by supergene alteration [46].

Since iron silicates in BIF are both ferrous and ferric, whereas goethite is exclusively ferric; the mineral replacement is triggered in an oxidative medium, permitting Fe^{2+} oxidation in situ, which is then directly incorporated in goethite under Fe^{3+} through the qualitative reaction (1). We infer here that the main oxidant is H_2O. The possible oxidation of iron by other oxidant species will be discussed Section 4.4.2.

$$2Fe^{2+}O_{silicate} + H_2O \Leftrightarrow Fe^{3+}_2O_{3\ goethite} + H_2 \qquad (1)$$

- Fe^{2+}-bearing oxide alteration

In the three samples, XRD analyses showed that magnetite is the main remaining Fe^{2+} bearing mineral, which can be explained by a slower oxidation compared to carbonates or silicates during weathering. Magnetite is often accompanied by the ferric oxide hematite such as in B3C. Microscopic observations realized in this zone revealed a more complex mineralogy (Figure 15) with essentially white-pinkish euhedral oxides stripped by even brighter lines. In the literature, this facies corresponds to kenomagnetite and maghemite (Figure 15b, [45]). They are known to develop as metastable phases during the on-going martitization process, a slow destabilization and oxidation of primary magnetite to hematite when BIF are progressively exhumed [16]. Due to the similar properties of kenomagnetite/maghemite and magnetite/hematite (same crystalline system and/or same chemical element and/or same oxidation degree), it is difficult to discriminate these phases. This explains the XRD results, which only showed hematite and magnetite presence for this sample. In parallel, goethite has also been observed in veins originating from kenomagnetite/maghemite, showing a dissolution pattern (Figure 15d). This can be interpreted as the mobilization of Fe^{2+} by alteration fluids in a low oxidative medium and its precipitation under Fe^{3+} in goethite veins when the environment becomes more oxidative closer to the surface. The oxidation of ferrous iron contained in magnetite could be summarized by the qualitative reaction (2). Like for Equation (1), we infer here that the main oxidant is H_2O.

$$2Fe^{2+}O_{magnetite} + H_2O \Leftrightarrow Fe^{3+}{}_2O_{3\ goethite/hematite} + H_2 \tag{2}$$
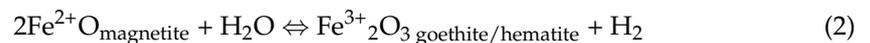
4.4.2. Is Water the Main Oxidant during BIF Alteration?

The petrographic study shows that BIF-hosted ore formations are the results of the circulation of oxidizing fluids. Some authors also mention deeper fluid circulation [47,48]. Although these fluid circulations leach and oxidize the rocks, the exact nature of the oxidant remains unclear. For example, some authors talked of a "deeply circulating heated meteoric fluid" able to "convert siderite-stilpnomelane to an ankerite-hematite assemblage" [48], but the redox reactions were not further investigated. In some papers, dissolved O_2 concentrations in circulating groundwater was taken as the main chemical parameter (in addition to physical parameters such as permeability), constraining the rate of BIF oxidation ([49] and references therein). Nonetheless, supergene alteration (and so oxidation) profiles can reach in some cases several hundreds of meters below the surface [50]. Is the circulating water still oxygenated at such depth? Numerous studies show that groundwater usually falls toward reducing conditions, since all conventional oxidants (such as O_2, NO_3^- or SO_4^{2-}) are quickly consumed in the first meters of soil/sediments by organic matter oxidation [51–53]. This favors water being the main oxidant, and thus the possibility for BIF-contained iron to be directly oxidized by water molecules is highly possible.

4.4.3. Fe^{2+}-Budget for H_2 Generation in Fresh BIF1 Sample

During BIF-hosted iron ore formation, it has been demonstrated that all Fe^{2+} is converted in Fe^{3+}. Thus, by using the iron content and Fe^{2+} remaining in the BIF1 sample, a first order estimate of H_2-generation remanent potential can be realized. As the lower part of this sample shows a higher oxidation rate related to water circulation, the focus has been made on the upper part of the sample (B1C and B1D). On the basis of the generic redox equation leading to iron oxidation and H_2 generation (3), H_2 potential from both $Fe^{2+}{}_{magnetite}$ and $Fe^{2+}{}_{silicate}$ in B1C and B1D have been evaluated. Detailed calculations are provided in Appendix C.

$$2Fe^{2+}O + H_2O \Leftrightarrow Fe^{3+}{}_2O_3 + H_2 \tag{3}$$
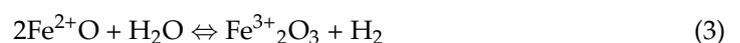
From B1C, which is an iron oxide rich level containing 56.83 wt% of total Fe and only magnetite as an Fe^{2+}-bearing mineral, the remanent H_2 generation potential through $Fe^{2+}{}_{magnetite}$ oxidation is evaluated to 100 mmol per kg of BIF from B1D, which is a quartz-rich level containing 14.08 wt% of total Fe with Fe^{2+} distributed in both magnetite and

silicates; the remanent H_2 generation potential through $Fe^{2+}_{magnetite}$ and $Fe^{2+}_{silicate}$ oxidations are evaluated to be 200 mmol and 70 mmol per kg of BIF, respectively. Studies showed that H_2 is produced from <100 mmol to >300 mmol per kg of dunite or harzburgite during serpentinization, depending on the temperature [54]. The comparison with our first order estimates demonstrates the potential of fresh BIF for H_2 generation. Finally, although H_2 potential seems much higher for magnetite than silicate in the first instance, since magnetite is the major Fe^{2+}-bearing mineral in BIF, the kinetics of reaction for martitization might require a longer time as transitionary stages exist, whereas Fe^{2+}-silicates are more easily weathered during BIF weathering.

4.4.4. Is There a Temporal Concordance between BIF Alteration and H_2 Emissions?

The BIF surficial alteration profiles and related ore bodies worldwide are associated with past or present lateritization processes in tropical climates. Since the break-up of Pangea 200 My ago, the on-going continental drift induces a continuous evolving new climate setting for continents. Some studies demonstrated that the Australian drift triggered major climate changes in the continent due to entering the intertropical zone during the Cenozoic, with tropical conditions that mainly lasted during the Miocene [50]. Hence, it is not surprising to find BIF-hosted iron ores dated back to the Cenozoic in Australia [55]. The lateritization of BIF in Western Australia is likely to be stopped or highly reduced nowadays, and so our samples are representative of a past surficial alteration and possible H_2 generation, which is not in agreement with active H_2 emitting SCD. Nonetheless, the current degassing of past-produced H_2 trapped under impermeable caps such as salt layers as well as in fluid inclusions within BIF rocks is a path to explore.

In parallel, although we did not focus on it during this study, the on-going oxidation of BIF-contained iron likely continues, independently of the lateritization processes, in deeper environments where basinal aqueous fluids circulate. It could be the case in the São Francisco Basin and western Australia where BIF do not outcrop but are suspected below sub-circular depressions.

4.4.5. Kinetic Factors Concern for H_2 Generation by BIF Oxidation

This study promoted promising elements for H_2 generation by water reduction and iron oxidation during BIF alteration. These water–rock interactions are mainly associated with supergene alteration profiles reaching tens or maximum hundreds of meters [56]. Although the generation of H_2 at such low depths (and so almost ambient T°) would not be of economic interest due to a lack of traps, it challenges the idea that high P/T conditions are required to generate H_2 through iron redox reactions. For example, the serpentinization of basic rocks has been widely studied through calculations and experiments showing an optimal temperature for H_2 generation around 300 °C [57]. Experiments at near-atmospheric temperature were also investigated and showed that H_2 can be formed with the presence of catalysts such as magnetite [58]. In parallel, only few works focused on H_2 generation through the oxidation of iron contained in other families of minerals so far. Some of them demonstrated the possibility of H_2 generation by wate–rrock interactions with siderite at 200–300 °C [59], but the generation at lower temperature has not yet been tested.

In Western Australia, a recent work promoted low generation temperatures of H_2 thanks to the geothermometer H_2-CH_4, despite the mechanisms leading to the formation of these gases remain unclear [33]. For BIF, the generation of natural H_2 by iron oxidation at these low range of temperatures might require catalysts of biological as well as chemical origins, like it has been proposed in serpentinization contexts. For example, authors pointed out that H_2 generation efficiency can be highly dependent on pH [60], Ni of Pd presence [57], the abundance of magnetite [58] or chemical composition of rocks [61]. The role of microorganisms to facilitate the reaction should also be studied.

4.5. Synthesis of the Petrographic Study: A Model of BIF Samples Alteration and Related H_2 Generation

BIF constitute a massive ferrous iron reservoir when preserved from surficial alteration, but their exhumation induces a strong leaching that can reach few hundreds of meters in depth [56]. This leads to a quasi-complete iron oxidation and formation of BIF-hosted iron ores, which are dated to a recent past (Cenozoic) in the case of Western Australia [50,62]. The petrological work on samples from Western Australia in transitional stages between fresh and weathered showed that both primary ferrous oxides and primary ferrous silicates/carbonates are sensitive to oxidizing fluid circulation. On the basis of an iron ore formation model that has been proposed in literature [56], the sketch presented in Figure 16 proposes a conceptual petrological history of the samples related to H_2 generation. It must be noticed that the kinetics and depth of H_2 generation are not constrained yet, and additional data and modeling will be necessary. Martitization and goethitization are processes that are observed in several geological contexts [16,45], but thermodynamic (and subsequently kinetic) data are needed to verify that the proposed reactions may have an impact of the gas signature in the studied basins.
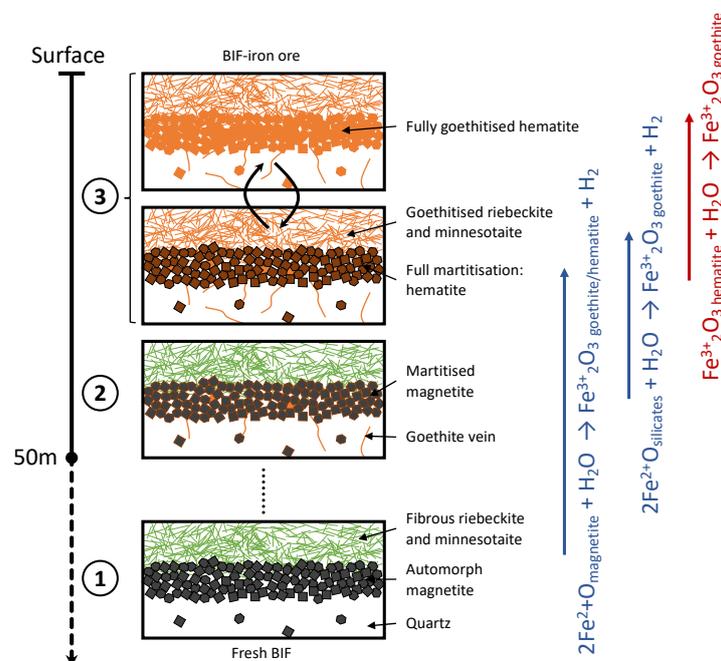
Figure 16. A possible petrological history of the samples and related H_2 generation. Fe^{2+}-bearing minerals such as magnetite and riebeckite/minnesotaite are altered by water circulation and ferrous iron oxidizes to generate H_2. Fe^{3+}-bearing minerals such as hematite are altered by water circulation to form oxi-hydroxide goethite, but no H_2 is generated during this mineral transition.

1. The BIF samples are made up of alternating layers of quartz and primary automorphy magnetite. In the quartz layers, various proportions of minor phases such as primary iron silicates and primary iron oxides occur;
2. When weathering starts, the BIF undertakes an oxidation episode, underlined by the presence of kenomagnetite and maghemite, which mark the on-going martitization process of the primary magnetite. The martitization can be accompanied by a mobilization of Fe^{2+} in circulation fluids before reprecipitation as Fe^{3+} in goethite veins closer to the surface when the medium become more oxidizing. Quartz starts being dissolved, increasing progressively the permeability and hence fluid circulation;
3. A second oxidative alteration episode occurs closer to the surface, when fluid circulation intensifies. The minor phases such as iron silicates or carbonates are destabilized

and ferric iron precipitates in situ as goethite pseudomorph, or ex situ in voids created by the rock leaching.

5. Conclusions

One of the major processes leading to H_2 generation in the continental domain is the oxidation of iron coupled to the water reduction, mostly in basic or ultrabasic rocks containing high rates of ferrous iron in minerals such as olivine. Based on a work coupling both satellite images and petrological approaches, we proposed in this paper a new iron-rich lithology able to generate H_2 through iron oxidation: banded iron formations.

- Topography and sky images analyses

Rounded depressions have been known for a few years to be the expression of currently active H_2 emissions in the landscape and are now found worldwide [9,10,25]. Recently, a study promoted a statistical approach based on satellite imaging to better constrain the sub circular depressions (SCD) and proved H_2 emitting sub circular depressions (P_H2_SCD) morphologies and separate them from other circular features as karsts [12]. The work demonstrated the efficiency of the technique to target new regions to explore for H_2 emissions.

In this paper, satellite imaging revealed the presence of these structures around the BIF in several regions worldwide: Australia, South Africa and Brazil. In order to test the nature of these features, hundreds of them were mapped from five new areas of Australia and South Africa and were added to the previous dataset. The statistical approach validated the idea of probable on-going H_2 seeps in these regions that will need to be monitored by field measurements in the future, giving credit to the hypothesis of H_2 generation by oxidation of BIF-hosted iron.

- Petrological study

The role of BIF as a H_2 generator has never been explored yet, despite them standing as a major resource of ferrous iron on earth with Fe_{tot} content from 20 and 40 wt% and low Fe^{3+}/Fe_{tot} ratios (from 0.05 to 0.58) when they are preserved from alteration. In parallel, data from surficial altered BIF always exhibit high Fe^{3+}/Fe_{tot} ratios (very close to 1), involving a strong oxidation when BIF reach the surface.

We presented in this study the results of a petrological work conducted on weathered BIF samples from the Hamersley Province in Western Australia. The study revealed mineralogical transitions during supergene alteration, from ferrous/ferric silicates and oxides (riebeckite/minnesotaite and magnetite) to exclusively ferric oxides (hematite) and oxi-hydroxides (goethite). These replacements emphasize the oxidation by water–rock interactions, which are strong evidence of H_2 generation by BIF oxidation.

In addition, evidences presented here infer a H_2 potential at a very low depth, when BIF is weathered at the surface, implying a very low generation temperature (under 50 °C and 150 bar). On the contrary to redox iron transformations at higher temperatures, the ability for these transformations to produce reduced gas (H_2, CH_4) in anoxic conditions at lower temperatures, is still poorly constrained in onshore domains such as in ophiolitic contexts ([63] and references therein). Hence, the new observations in BIF context are a matter of debate and further studies. It also must not be excluded that BIF could react and oxidize when meeting underground water circulation in much deeper environments in the case of buried BIF under thick sedimentary layers, with higher P-T conditions.

Finally, a question of temporal concordance can be raised: Does currently H_2 emitted on fairy circles originate from BIF weathering in Western Australia, South Africa and Brazil? Such surficial alteration profiles are dated to the Cenozoic, the current era, and are related to major climate changes worldwide triggered by the break-up of Pangea [50]. Hence, it is possible that active SCD are related to still on-going surficial strong alteration of BIF where the climate is still tropical like in Brazil. In some other cases, such as in Australia, the lateritization of BIF is also Cenozoic but has decreased in the past My due to evolution of Australian climate dynamics related to the continental drift. Thus, this is more uncertain

to have an on-going H_2 generation by BIF surficial alteration. Nonetheless, the current emissions of H_2 might be related to the oxidation of BIF in deeper environments where aqueous fluids circulate as well as currently degassing past-produced H_2 trapped in rocks within fluid inclusions or under impermeable caps such as salt layers.

- Implications for the future of H_2 exploration

Even if the relationship between H_2 generation and BIF will require additional characterization, we proposed here to add the iron-rich lithology to the list of potential H_2 source rocks in the continental context. BIF are a worldwide-distributed lithology. As far as we know, the spatial correlation between BIF and supposed H_2 emanations can be pointed out on more numerous places than only Brazil, Australia or South-Africa. Thus, targeting BIF might be another proxy for natural H_2 exploration. Obviously, the targeted BIF for H_2 exploration could be in subsurfaces at the opposite of the ones targeted by the iron mine industry, which have to outcrop, or be close to thesurface. BIF constitute the main ferrous-iron resource on Earth, hence including this additional lithology, as a H_2 source in the global balance might significantly increase the annually estimates of emitted H_2 that are now 10^{13} mol/an according to the latest calculations [14]. Finally, the possibility of H_2 production at a relative ambient temperature has been suggested in this paper, concurring with a previous study [33]. If true, it might open a new whole field of research for H_2 generation, which has always been considered to require higher temperatures up to now.

Appendix A

Table A1. Chemical compositions (in oxide wt%) of the BIF1, BIF2 and BIF3 samples obtained by ICP-OES.

| Sample	Chemical Composition—ICP-OES (wt%)											
	SiO_2	Al_2O_3	Fe_2O_3	MnO	MgO	CaO	Na_2O	K_2O	TiO_2	P_2O_5	L.O.I. *	Total
B1A	71.06	0.11	16.83	<D.L.	1.37	1.07	1.04	<D.L.	<D.L.	<D.L.	2.72	94.19
B1B	57.55	0.05	21.60	0.027	0.13	10.54	0.12	<D.L.	<D.L.	<D.L.	9.61	99.61
B1C	15.78	0.29	81.18	<D.L.	0.88	0.50	0.10	0.12	<D.L.	0.35	0.38	99.58
B1D	73.95	0.51	20.11	<D.L.	2.62	0.04	0.08	0.23	<D.L.	<D.L.	2.29	99.83
B2A	32.32	0.25	60.81	<D.L.	<D.L.	0.03	<D.L.	<D.L.	<D.L.	0.10	6.50	100.01
B2B	55.00	0.05	41.35	<D.L.	<D.L.	<D.L.	<D.L.	<D.L.	<D.L.	<D.L.	3.24	99.63
B3A	58.18	<D.L.	38.59	0.23	0.09	0.04	<D.L.	<D.L.	<D.L.	0.10	2.66	99.88
B3B	43.30	<D.L.	52.67	0.19	0.19	0.04	<D.L.	<D.L.	<D.L.	<D.L.	2.84	99.23
B3C	39.78	<D.L.	59.57	<D.L.	<D.L.	0.04	<D.L.	<D.L.	<D.L.	<D.L.	−0.27	99.12

* L.O.I.: Loss on Ignition includes loss of volatiles and gain from oxidation of Fe^{2+}. D.L.: Detection Limit.

Appendix B
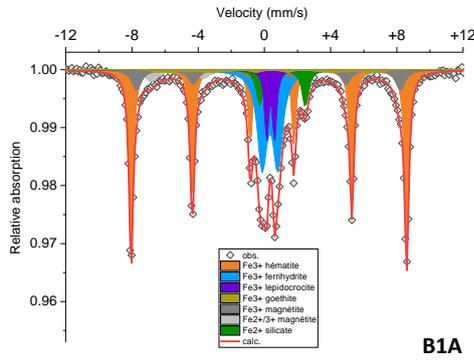
B1A	d (mm/s)	D ou 2ε (mm/s)	B_{hf} (T)	Γ (mm/s)	Area (%)	Attribution
S1	0.37(1)	-0.19(1)	51.6(1)	0.30(1)	43(3)	Fe³⁺ hematite
DQ1	0.34(2)	0.94(8)	-	0.69(5)	23(3)	Fe³⁺ ferrihydrite
DQ2	0.38(1)	0.48(3)	-	0.28(3)	7(3)	Fe³⁺ lepidocrocite
S2	0.37(2)	-0.15(6)	37.1*	0.40(-)	3(3)	Fe³⁺ goethite
S3	0.28(3)	-0.07(5)	49.4(5)	0.69(5)	10(3)	Fe³⁺ magnetite
S4	0.64(3)	-0.05(5)	46.3(6)	0.90(5)	8(3)	Fe²⁺/³⁺ magnetite
DQ3	1.09(3)	2.74(6)	-	0.47(5)	6(3)	Fe²⁺ silicate
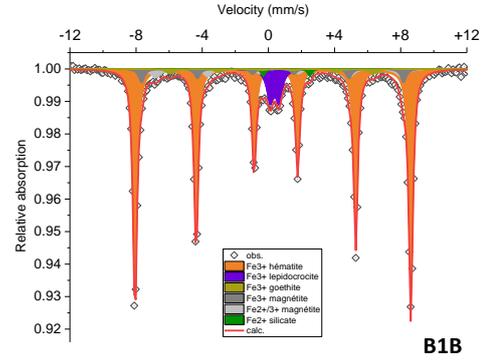
B1B	d (mm/s)	D ou 2ε (mm/s)	B_{hf} (T)	Γ (mm/s)	Area (%)	Attribution
S1	0.37(1)	-0.18(1)	51.7(1)	0.30(1)	76(3)	Fe³⁺ hematite
DQ2	0.37(2)	0.53(3)	-	0.45(5)	7(3)	Fe³⁺ lepidocrocite
S2	0.38(2)	-0.33(8)	38.1(8)	0.62(8)	3(3)	Fe³⁺ goethite
S3	0.28(3)	-0.04(4)	49.1(2)	0.40(3)	6(3)	Fe³⁺ magnetite
S4	0.63(6)	-0.01(2)	46.2(6)	0.50(3)	7(3)	Fe²⁺/³⁺ magnetite
DQ3	1.10(3)	2.81(5)	-	0.30(-)	< 3	Fe²⁺ silicate
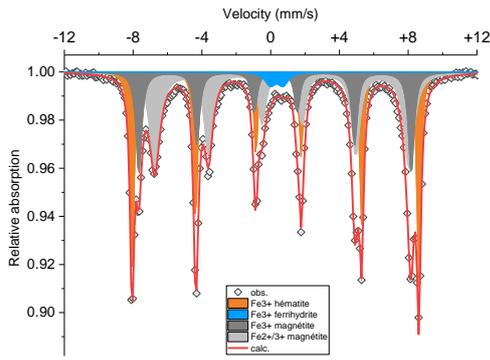
B1C	d (mm/s)	D ou 2ε (mm/s)	B_{hf} (T)	Γ (mm/s)	Area (%)	Attribution
S1	0.37(1)	-0.18(1)	51.7(1)	0.28(1)	34(3)	Fe³⁺ hematite
DQ2	0.35(2)	0.74(6)	-	0.66(7)	3(3)	Fe³⁺ ferrihydrite
S3	0.27(1)	-0.04(1)	49.1(4)	0.40(4)	24(3)	Fe³⁺ magnetite
S4	0.66(1)	-0.01(1)	45.9(4)	0.53(2)	39(3)	Fe²⁺/³⁺ magnetite
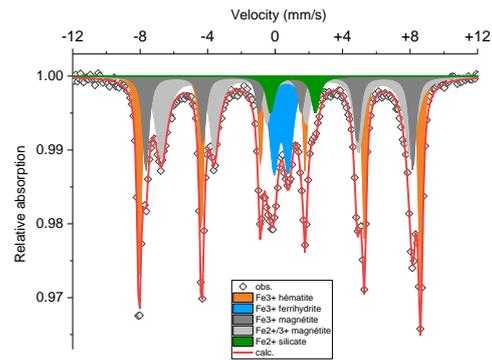
B1D	d (mm/s)	D ou 2ε (mm/s)	B_{hf} (T)	Γ (mm/s)	Area (%)	Attribution
S1	0.37(1)	-0.18(1)	51.7(1)	0.28(1)	30(3)	Fe³⁺ hematite
DQ2	0.36(2)	0.84(3)	-	0.65(5)	13(3)	Fe³⁺ ferrihydrite
S3	0.27(1)	-0.04(2)	49.0(4)	0.42(3)	19(3)	Fe³⁺ magnetite
S4	0.66(1)	-0.03(2)	45.8(4)	0.59(3)	33(3)	Fe²⁺/³⁺ magnetite
DQ3	1.05(3)	2.66(6)	-	0.54(8)	5(3)	Fe²⁺ silicate
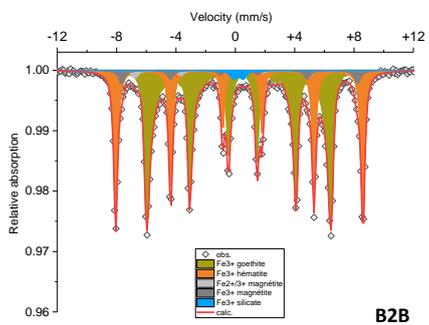
9	d (mm/s)	D ou 2ε (mm/s)	B_{hf} (T)	Γ (mm/s)	Area (%)	Attribution
S1	0.37(1)	-0.20(1)	51.7(2)	0.29(1)	35(3)	Fe³⁺ (hématite)
S2	0.26(2)	0.05(4)	49.3(4)	0.48(2)	4(3)	Fe³⁺ tét. (magnétite)
S3	0.67(2)	0.04(3)	46.2(4)	0.50(2)	3(3)	Fe²⁺/³⁺ oct. (magnétite)
S4	0.37(2)	-0.27(3)	36*	0.30(-)	56(3)	Fe³⁺ (goethite)
DQ1	0.21(3)	0.64(4)	-	0.54(4)	< 3	Fe³⁺ tét. (silicate)
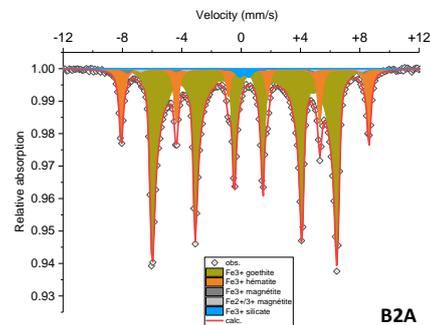
11	d (mm/s)	D ou 2ε (mm/s)	B_{hf} (T)	Γ (mm/s)	Area (%)	Attribution
S1	0.37(1)	-0.20(1)	51.8(2)	0.32(2)	18(3)	Fe³⁺ (hématite)
S2	0.26(2)	0.05(4)	49.3(4)	0.48(2)	< 3	Fe³⁺ tét. (magnétite)
S3	0.67(2)	0.04(3)	46.2(4)	0.50(2)	< 3	Fe²⁺/³⁺ oct. (magnétite)
S4	0.37(1)	-0.27(1)	36*	0.30(-)	78(3)	Fe³⁺ (goethite)
DQ1	0.21(3)	0.64(4)	-	0.54(4)	< 3	Fe³⁺ tét. (silicate)

Figure A1. Mössbauer spectra and data for BIF1, BIF2 and BIF3 samples.
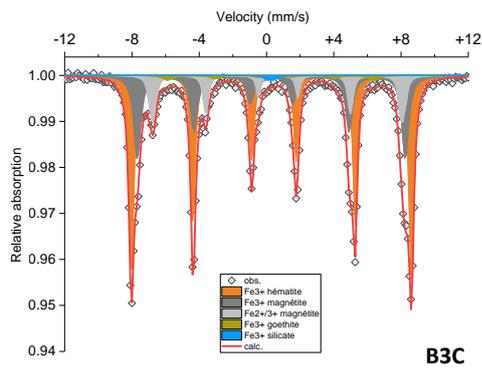
1	d (mm/s)	D ou 2ε (mm/s)	B_{hf} (T)	Γ (mm/s)	Area (%)	Attribution
S1	0.37(1)	−0.16(4)	51.6(3)	0.34(1)	52(3)	Fe^{3+} (hematite)
S2	0.29(2)	−0.01(5)	49.4(5)	0.49(4)	30(3)	Fe^{3+} tet. (magnetite)
S3	0.67(2)	−0.04(5)	46.1(5)	0.45(4)	15(3)	$Fe^{2+/3+}$ oct. (magnetite)
S4	0.37(2)	−0.24(6)	38.1(5)	0.68(4)	< 3	Fe^{3+} (goethite)
DQ1	0.23(3)	0.4(1)	-	0.50(4)	< 3	Fe^{3+} tet. (silicate)
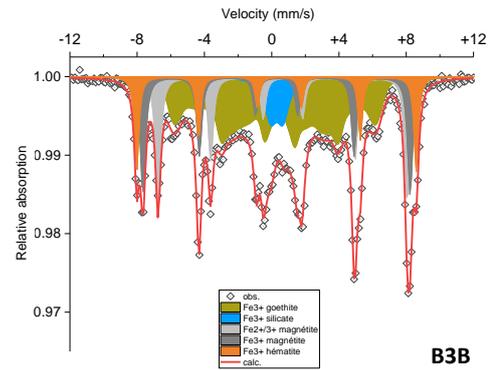
4	d (mm/s)	D ou 2ε (mm/s)	B_{hf} (T)	Γ (mm/s)	Area (%)	Attribution
S1	0.37(1)	−0.17(3)	51.5(2)	0.32(1)	13(3)	Fe^{3+} (hematite)
S2	0.29(2)	−0.01(4)	49.3(3)	0.37(2)	18(3)	Fe^{3+} tet. (magnetite)
S3	0.66(2)	−0.01(4)	45.9(3)	0.37(2)	19(3)	$Fe^{2+/3+}$ oct. (magnetite)
S4	0.34(2)	−0.27(6)	27*	0.30(-)	43(3)	Fe^{3+} (goethite)
DQ1	0.28(3)	0.7(1)	-	0.88(5)	7(3)	Fe^{3+} tet. (silicate)
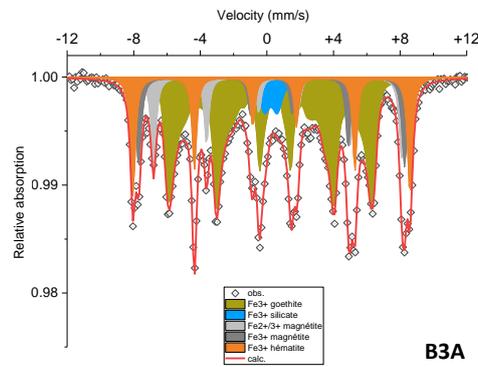
6	d (mm/s)	D ou 2ε (mm/s)	B_{hf} (T)	Γ (mm/s)	Area (%)	Attribution
S1	0.37(1)	−0.19(3)	51.6(2)	0.35(1)	18(3)	Fe^{3+} (hematite)
S2	0.27(2)	0.02(3)	49.5(3)	0.36(2)	14(3)	Fe^{3+} tet. (magnetite)
S3	0.67(2)	−0.04(3)	46.3(3)	0.37(2)	13(3)	$Fe^{2+/3+}$ oct. (magnetite)
S4	0.36(2)	−0.28(4)	32*	0.30(-)	50(3)	Fe^{3+} (goethite)
DQ1	0.25(3)	0.78(5)	-	0.75(5)	5(3)	Fe^{3+} tet. (silicate)

Figure A2. Mössbauer spectra and data for BIF1, BIF2 and BIF3 samples.

Appendix C

B1C sample: total Fe content = 56.8 wt%, $Fe^{2+}_{magnetite}$ = 39 % /2 = 19.5 %

- **magnetite** :

  ⇒ Corresponding to : Fe^{2+} content in the sample = 56.8 × 19.5% = 11.1 wt%

  ($\rightarrow$ Molar mass ratio $Fe/FeO = 0.78$)

  ⇒ Corresponding to : FeO content in the sample = 11.1/0.78 = 14.0 wt% FeO = 140 g FeO/ kg rock

  ($\rightarrow$ Molar mass $FeO = 71.8$ g/mol)

  ⇒ Corresponding to : FeO mass in the sample = 140/71.8 ≈ 2 mol FeO / kg rock

  ($\rightarrow$ 2 mol FeO generate 1 mol H_2)

  ⇒ Corresponding to : ≈ 1 mol H_2/ kg rock ≈ 1000 mmol H_2/ kg rock

B1D sample: total Fe content = 14.1 wt%, $Fe^{2+}_{magnetite}$ = 33 % /2 = 16.5 %, $Fe^{2+}_{silicate}$ = 5 %

- **magnetite** :

  ⇒ Corresponding to : Fe^{2+} content in the sample = 14.1 ×16.5% = 2.32$wt\%$

  ($\rightarrow$ Molar mass ratio $Fe/FeO = 0.78$)

  ⇒ Corresponding to : FeO content in the sample = 2.32/0.78 = 3.00 wt% FeO = 30.0 g FeO/ kg rock

  ($\rightarrow$ Molar mass $FeO = 71.8$ g/mol)

  ⇒ Corresponding to : FeO mass in the sample = 30.0/71.8 ≈ 0.4 mol FeO / kg rock

  ($\rightarrow$ 2 mol FeO generate 1 mol H_2)

  ⇒ Corresponding to : ≈ 0.2 mol H_2/ kg rock ≈ 200 mmol H_2/ kg rock

- **silicate** :

  ⇒ Corresponding to : Fe^{2+} content in the sample = 14.08 ×5% = 0.70$wt\%$

  ($\rightarrow$ Molar mass ratio $Fe/FeO = 0.78$)

  ⇒ Corresponding to : FeO content in the sample = 0.70/0.78 = 0.91 wt% FeO = 9.10 g FeO/ kg rock

  ($\rightarrow$ Molar mass $FeO = 71.8$ g/mol)

  ⇒ Corresponding to : FeO mass in the sample = 9.10/71.8 ≈ 0.13 mol FeO / kg rock

  ($\rightarrow$ 2 mol FeO generate 1 mol H_2)

  ⇒ Corresponding to : ≈ 0.07 mol H_2/ kg rock ≈ 70mmol mol H_2/ kg rock

Figure A3. Detailed calculations for first-order estimates of H_2 generation potential of fresh BIF1 sample.

References

1. Prinzhofer, A.; Deville, É. *Hydrogène Naturel: La Prochaine Révolution Energétique?* Belin: Paris, France, 2015; ISBN 978-2-7011-8384-8.
2. Truche, L.; McCollom, T.M.; Martinez, I. Hydrogen and Abiotic Hydrocarbons: Molecules That Change the World. *Elements* **2020**, *16*, 13–18. [CrossRef]
3. Krasnov, S.G.; Cherkashev, G.A.; Stepanova, T.V.; Batuyev, B.N.; Krotov, A.G.; Malin, B.V.; Maslov, M.N.; Markov, V.F.; Poroshina, I.M.; Samovarov, M.S.; et al. Detailed Geological Studies of Hydrothermal Fields in the North Atlantic. *Geol. Soc. Lond. Spec. Publ.* **1995**, *87*, 43–64. [CrossRef]
4. Charlou, J.L.; Donval, J.P.; Fouquet, Y.; Jean-Baptiste, P.; Holm, N. Geochemistry of High H_2 and CH_4 Vent Fluids Issuing from Ultramafic Rocks at the Rainbow Hydrothermal Field (36j14VN, MAR). *Chem. Geol.* **2002**, *191*, 345–359. [CrossRef]

5. Welhan, J.A.; Craig, H. Methane and Hydrogen in East Pacific Rise Hydrothermal Fluids. *Geophys. Res. Lett.* **1979**, *6*, 829–831. [CrossRef]
6. Guélard, J.; Beaumont, V.; Rouchon, V.; Guyot, F.; Pillot, D.; Jézéquel, D.; Ader, M.; Newell, K.D.; Deville, E. Natural H_2 in Kansas: Deep or Shallow Origin? *Geochem. Geophys. Geosyst.* **2017**, *18*, 1841–1865. [CrossRef]
7. Prinzhofer, A.; Cissé, C.S.T.; Diallo, A.B. Discovery of a Large Accumulation of Natural Hydrogen in Bourakebougou (Mali). *Int. J. Hydrog. Energy* **2018**, *43*, 19315–19326. [CrossRef]
8. Etiope, G.; Schoell, M.; Hosgörmez, H. Abiotic Methane Flux from the Chimaera Seep and Tekirova Ophiolites (Turkey): Understanding Gas Exhalation from Low Temperature Serpentinization and Implications for Mars. *Earth Planet. Sci. Lett.* **2011**, *310*, 96–104. [CrossRef]
9. Prinzhofer, A.; Moretti, I.; Françolin, J.; Pacheco, C.; D'Agostino, A.; Werly, J.; Rupin, F. Natural Hydrogen Continuous Emission from Sedimentary Basins: The Example of a Brazilian H_2-Emitting Structure. *Int. J. Hydrog. Energy* **2019**, *44*, 5676–5685. [CrossRef]
10. Zgonnik, V.; Beaumont, V.; Deville, E.; Larin, N.; Pillot, D.; Farrell, K.M. Evidence for Natural Molecular Hydrogen Seepage Associated with Carolina Bays (Surficial, Ovoid Depressions on the Atlantic Coastal Plain, Province of the USA). *Prog. Earth Planet. Sci.* **2015**, *2*, 31. [CrossRef]
11. Lollar, B.S.; Onstott, T.C.; Lacrampe-Couloume, G.; Ballentine, C.J. The Contribution of the Precambrian Continental Lithosphere to Global H_2 Production. *Nature* **2014**, *516*, 379–382. [CrossRef]
12. Moretti, I.; Brouilly, E.; Loiseau, K.; Prinzhofer, A.; Deville, E. Hydrogen Emanations in Intracratonic Areas: New Guide Lines for Early Exploration Basin Screening. *Geosciences* **2021**, *11*, 145. [CrossRef]
13. Moretti, I.; Prinzhofer, A.; Françolin, J.; Pacheco, C.; Rosanne, M.; Rupin, F.; Mertens, J. Long-Term Monitoring of Natural Hydrogen Superficial Emissions in a Brazilian Cratonic Environment. Sporadic Large Pulses versus Daily Periodic Emissions. *Int. J. Hydrog. Energy* **2021**, *46*, 3615–3628. [CrossRef]
14. Zgonnik, V. The Occurrence and Geoscience of Natural Hydrogen: A Comprehensive Review. *Earth Sci. Rev.* **2020**, *203*, 103140. [CrossRef]
15. Klein, C.; Beukes, N.J. Sedimentology and Geochemistry of the Glaciogenic Late Proterozoic Rapitan Iron-Formation in Canada. *Econ. Geol.* **1993**, *88*, 542–565. [CrossRef]
16. Ramanaidou, E.R.; Wells, M.A. Sedimentary Hosted Iron Ores. In *Treatise on Geochemistry*; Elsevier: Amsterdam, The Netherlands, 2014; pp. 313–355. ISBN 978-0-08-098300-4.
17. Ilyin, A.V. Neoproterozoic Banded Iron Formations. *Lithol. Miner. Resour.* **2009**, *44*, 78–86. [CrossRef]
18. Bekker, A.; Slack, J.F.; Planavsky, N.; Krapez, B.; Hofmann, A.; Konhauser, K.O.; Rouxel, O.J. Iron Formation: The Sedimentary Product of a Complex Interplay among Mantle, Tectonic, Oceanic, and Biospheric Processes. *Econ. Geol.* **2010**, *105*, 467–508. [CrossRef]
19. Cox, G.M.; Halverson, G.P.; Minarik, W.G.; Le Heron, D.P.; Macdonald, F.A.; Bellefroid, E.J.; Strauss, J.V. Neoproterozoic Iron Formation: An Evaluation of Its Temporal, Environmental and Tectonic Significance. *Chem. Geol.* **2013**, *362*, 232–249. [CrossRef]
20. Zhu, X.-Q.; Tang, H.-S.; Sun, X.-H. Genesis of Banded Iron Formations: A Series of Experimental Simulations. *Ore Geol. Rev.* **2014**, *63*, 465–469. [CrossRef]
21. Angerer, T.; Duuring, P.; Hagemann, S.G.; Thorne, W.; McCuaig, T.C. A Mineral System Approach to Iron Ore in Archaean and Palaeoproterozoic BIF of Western Australia. *Geol. Soc. Lond. Spec. Publ.* **2015**, *393*, 81–115. [CrossRef]
22. Klein, C. Some Precambrian Banded Iron-Formations (BIFs) from around the World: Their Age, Geologic Setting, Mineralogy, Metamorphism, Geochemistry, and Origins. *Am. Mineral.* **2005**, *90*, 1473–1499. [CrossRef]
23. Myagkiy, A.; Brunet, F.; Popov, C.; Krüger, R.; Guimarães, H.; Sousa, R.S.; Charlet, L.; Moretti, I. H_2 Dynamics in the Soil of a H_2-Emitting Zone (São Francisco Basin, Brazil): Microbial Uptake Quantification and Reactive Transport Modelling. *Appl. Geochem.* **2020**, *112*, 104474. [CrossRef]
24. Myagkiy, A.; Moretti, I.; Brunet, F. Space and Time Distribution of Subsurface H_2 Concentration in so-Called "Fairy Circles": Insight from a Conceptual 2-D Transport Model. *BSGF Earth Sci. Bull.* **2020**, *191*, 13. [CrossRef]
25. Larin, N.; Zgonnik, V.; Rodina, S.; Deville, E.; Prinzhofer, A.; Larin, V.N. Natural Molecular Hydrogen Seepage Associated with Surficial, Rounded Depressions on the European Craton in Russia. *Nat. Resour. Res.* **2015**, *24*, 369–383. [CrossRef]
26. Rezaee, R. Natural Hydrogen System in Western Australia? *Earth Sci.* **2020**, 2020100589. [CrossRef]
27. Frery, E.; Langhi, L.; Maison, M.; Moretti, I. Natural Hydrogen Seeps Identified in the North Perth Basin, Western Australia. *Int. J. Hydrog. Energy* **2021**, *46*, 31158–31173. [CrossRef]
28. Tschinkel, W.R. Experiments Testing the Causes of Namibian Fairy Circles. *PLoS ONE* **2015**, *10*, e0140099. [CrossRef]
29. Preiss, W.V. The Adelaide Geosyncline of South Australia and Its Significance in Neoproterozoic Continental Reconstruction. *Precambrian Res.* **2000**, *100*, 21–63. [CrossRef]
30. Betts, P.; Giles, D. The 1800–1100Ma Tectonic Evolution of Australia. *Precambrian Res.* **2006**, *144*, 92–125. [CrossRef]
31. Ward, L. Inflammable Gases Occluded in the Pre-Palaeozoic Rocks of South Australia. *Trans. Proc. R. Soc. S. Aust.* **1933**, *57*, 42–47.
32. Boreham, C.J.; Edwards, D.S.; Czado, K.; Rollet, N.; Wang, L.; van der Wielen, S.; Champion, D.; Blewett, R.; Feitz, A.; Henson, P.A. Hydrogen in Australian Natural Gas: Occurrences, Sources and Resources. *APPEA J.* **2021**, *61*, 163. [CrossRef]
33. Boreham, C.J.; Sohn, J.H.; Cox, N.; Williams, J.; Hong, Z.; Kendrick, M.A. Hydrogen and Hydrocarbons Associated with the Neoarchean Frog's Leg Gold Camp, Yilgarn Craton, Western Australia. *Chem. Geol.* **2021**, *575*, 120098. [CrossRef]

34. Compston, W.; Kröner, A. Multiple Zircon Growth within Early Archaean Tonalitic Gneiss from the Ancient Gneiss Complex, Swaziland. *Earth Planet. Sci. Lett.* **1988**, *87*, 13–28. [CrossRef]

35. Scoates, J.S.; Friedman, R.M. Precise Age of the Platiniferous Merensky Reef, Bushveld Complex, South Africa, by the U-Pb Zircon Chemical Abrasion ID-TIMS Technique. *Econ. Geol.* **2008**, *103*, 465–471. [CrossRef]

36. Sodoudi, F.; Yuan, X.; Kind, R.; Lebedev, S.; Adam, J.M.-C.; Kästle, E.; Tilmann, F. Seismic Evidence for Stratification in Composition and Anisotropic Fabric within the Thick Lithosphere of Kalahari Craton: Thick and Layered Mantle Lithosphere. *Geochem. Geophys. Geosyst.* **2013**, *14*, 5393–5412. [CrossRef]

37. Reis, H.L.S.; Alkmim, F.F.; Fonseca, R.C.S.; Nascimento, T.C.; Suss, J.F.; Prevatti, L.D. The São Francisco Basin. In *São Francisco Craton, Eastern Brazil*; Heilbron, M., Cordani, U.G., Alkmim, F.F., Eds.; Regional Geology Reviews; Springer International Publishing: Cham, Switzerland, 2017; pp. 117–143. ISBN 978-3-319-01714-3.

38. Duuring, P.; Hagemann, S.G.; Laukamp, C.; Chiarelli, L. Supergene Modification of Magnetite and Hematite Shear Zones in Banded Iron-Formation at Mt Richardson, Yilgarn Craton, Western Australia. *Ore Geol. Rev.* **2019**, *111*, 102995. [CrossRef]

39. Auler, A.S.; Barton, H.A.; Zambelli, B.; Senko, J.; Parker, C.W.; Sasowsky, I.D.; Souza, T.A.R.; Pujoni, D.; Peñaranda, J.; Davis, R. Silica and Iron Mobilization, Cave Development and Landscape Evolution in Iron Formations in Brazil. *Geomorphology* **2022**, *398*, 108068. [CrossRef]

40. Donzé, F.-V.; Truche, L.; Shekari Namin, P.; Lefeuvre, N.; Bazarkina, E.F. Migration of Natural Hydrogen from Deep-Seated Sources in the São Francisco Basin, Brazil. *Geosciences* **2020**, *10*, 346. [CrossRef]

41. Webb, A.D.; Dickens, G.R.; Oliver, N.H.S. From Banded Iron-Formation to Iron Ore: Geochemical and Mineralogical Constraints from across the Hamersley Province, Western Australia. *Chem. Geol.* **2003**, *197*, 215–251. [CrossRef]

42. Ewers, W.E.; Morris, R.C. Studies of the Dales Gorge Member of the Brockman Iron Formation, Western Australia. *Econ. Geol.* **1981**, *76*, 1929–1953. [CrossRef]

43. Sun, S.; Li, Y.-L. Geneses and Evolutions of Iron-Bearing Minerals in Banded Iron Formations of >3760 to ca. 2200 Million-Year-Old: Constraints from Electron Microscopic, X-Ray Diffraction and Mössbauer Spectroscopic Investigations. *Precambrian Res.* **2017**, *289*, 1–17. [CrossRef]

44. Van Alboom, A.; De Grave, E. Temperature Dependence of the 57Fe Mössbauer Parameters in Riebeckite. *Phys. Chem. Miner.* **1996**, *23*, 377–386. [CrossRef]

45. Morris, R.C.; Ramanaidou, E.R. Genesis of the Channel Iron Deposits (CID) of the Pilbara Region, Western Australia. *Aust. J. Earth Sci.* **2007**, *54*, 733–756. [CrossRef]

46. Morris, R.C.; Kneeshaw, M. Genesis Modelling for the Hamersley BIF-Hosted Iron Ores of Western Australia: A Critical Review. *Aust. J. Earth Sci.* **2011**, *58*, 417–451. [CrossRef]

47. McLellan, J.G.; Oliver, N.H.S.; Schaubs, P.M. Fluid Flow in Extensional Environments; Numerical Modelling with an Application to Hamersley Iron Ores. *J. Struct. Geol.* **2004**, *26*, 1157–1171. [CrossRef]

48. Taylor, D.; Dalstra, H.J.; Harding, A.E.; Broadbent, G.C.; Barley, M.E. Genesis of High-Grade Hematite Orebodies of the HamersleyProvince, Western Australia. *Econ. Geol.* **2001**, *96*, 837–873. [CrossRef]

49. Robbins, L.J.; Funk, S.P.; Flynn, S.L.; Warchola, T.J.; Li, Z.; Lalonde, S.V.; Rostron, B.J.; Smith, A.J.B.; Beukes, N.J.; de Kock, M.O.; et al. Hydrogeological Constraints on the Formation of Palaeoproterozoic Banded Iron Formations. *Nat. Geosci.* **2019**, *12*, 558–563. [CrossRef]

50. Tardy, Y.; Kobilsek, B.; Paquet, H. Mineralogical Composition and Geographical Distribution of African and Brazilian Periatlantic Laterites. The Influence of Continental Drift and Tropical Paleoclimates during the Past 150 Million Years and Implications for India and Australia. *J. Afr. Earth Sci.* **1991**, *12*, 283–295. [CrossRef]

51. Canfield, D.E.; Jørgensen, B.B.; Fossing, H.; Glud, R.; Gundersen, J.; Ramsing, N.B.; Thamdrup, B.; Hansen, J.W.; Nielsen, L.P.; Hall, P.O.J. Pathways of Organic Carbon Oxidation in Three Continental Margin Sediments. *Mar. Geol.* **1993**, *113*, 27–40. [CrossRef]

52. Jørgensen, B.B.; Kasten, S. Sulfur Cycling and Methane Oxidation. In *Marine Geochemistry*; Schulz, H.D., Zabel, M., Eds.; Springer: Berlin/Heidelberg, Germany, 2006; pp. 271–309. ISBN 978-3-540-32143-9.

53. Lahiri, C.; Davidson, G.R. Heterogeneous Oxygenation of Wetland Soils with Increasing Inundation: Redox Potential, Water Depth, and Preferential Flow Paths. *Hydrol. Processes* **2020**, *34*, 1350–1358. [CrossRef]

54. Albers, E.; Bach, W.; Pérez-Gussinyé, M.; McCammon, C.; Frederichs, T. Serpentinization-Driven H_2 Production from Continental Break-Up to Mid-Ocean Ridge Spreading: Unexpected High Rates at the West Iberia Margin. *Front. Earth Sci.* **2021**, *9*, 673063. [CrossRef]

55. Angerer, T.; Hagemann, S.G.; Danyushevsky, L. High-Grade Iron Ore at Windarling, Yilgarn Craton: A Product of Syn-Orogenic Deformation, Hypogene Hydrothermal Alteration and Supergene Modification in an Archean BIF-Basalt Lithostratigraphy. *Min. Depos.* **2013**, *48*, 697–728. [CrossRef]

56. Morris, R.C. Genesis of Iron Ore in Banded Iron Formations by Supergene and Supergene Metamorphic Processes—A Conceptual Model. In *Regional Studies and Specific Deposits*; Elsevier: Amsterdam, The Netherlands, 1985; pp. 73–235. ISBN 978-0-444-42497-6.

57. Brunet, F. Hydrothermal Production of H_2 and Magnetite from Steel Slags: A Geo-Inspired Approach Based on Olivine Serpentinization. *Front. Earth Sci.* **2019**, *7*, 17. [CrossRef]

58. Neubeck, A.; Duc, N.T.; Bastviken, D.; Crill, P.; Holm, N.G. Formation of H_2 and CH_4 by Weathering of Olivine at Temperatures between 30 and 70 °C. *Geochem. Trans.* **2011**, *12*, 6. [CrossRef] [PubMed]

59. Milesi, V.; Guyot, F.; Brunet, F.; Richard, L.; Recham, N.; Benedetti, M.; Dairou, J.; Prinzhofer, A. Formation of CO_2, H_2 and Condensed Carbon from Siderite Dissolution in the 200–300 °C Range and at 50MPa. *Geochim. Cosmochim. Acta* **2015**, *154*, 201–211. [CrossRef]

60. Crouzet, C.; Brunet, F.; Recham, N.; Findling, N.; Lanson, M.; Guyot, F.; Ferrasse, J.-H.; Goffé, B. Hydrogen Production by Hydrothermal Oxidation of FeO under Acidic Conditions. *Int. J. Hydrog. Energy* **2017**, *42*, 795–806. [CrossRef]

61. Klein, F.; Bach, W.; McCollom, T.M. Compositional Controls on Hydrogen Generation during Serpentinization of Ultramafic Rocks. *Lithos* **2013**, *178*, 55–69. [CrossRef]

62. Ramanaidou, E.R.; Danišik, M.; Wells, M.A. Preliminary Dating of Martite Goethite Iron Ore in the Hamersley Province (Western Australia). *ASEG Ext. Abstr.* **2019**, *2019*, 1–2. [CrossRef]

63. Mayhew, L.E.; Ellison, E.T.; Miller, H.M.; Kelemen, P.B.; Templeton, A.S. Iron Transformations during Low Temperature Alteration of Variably Serpentinized Rocks from the Samail Ophiolite, Oman. *Geochim. Cosmochim. Acta* **2018**, *222*, 704–728. [CrossRef]